separations

MDPI

Article

Detoxification and Targeted Conversion of Waste Lithium Battery Electrolyte to Light Hydrocarbons via In Situ Catalytic Pyrolysis: Roles of Li, Ni, Co, and Mn Elements

Jingyi Wang, Yu Zhang and Lingen Zhang *

School of Environmental and Chemical Engineering, Shanghai University, 99 Shangda Road, Shanghai 200444, China; wangjingyi@shu.edu.cn (J.W.); 2576174129@shu.edu.cn (Y.Z.)
* Correspondence: lezhang@shu.edu.cn

Abstract

Spent lithium-ion battery electrolytes contain fluorine-, sulfur-, and phosphorus-bearing toxins, necessitating deep detoxification and directional conversion into C_1–C_6 light hydrocarbons. To elucidate the specific catalytic roles and sequential activation of cathode metals (Li, Ni, Co, Mn), this work systematically deconvolutes their mono- and multi-metallic migration mechanisms over a CaO-ZSM-5* catalyst during vacuum catalytic pyrolysis (530 °C, 100 Pa). Results reveal that Li^+ and Ni^{2+} dominate C–O bond cleavage in carbonates and CaO-ZSM-5*-assisted decarboxylation and oxygen fixation, significantly increasing the relative hydrocarbon content. Conversely, $Co^{2/3+}$ and Mn^{4+} release reactive oxygen species, causing deep oxidation of hydrocarbons into CO_2 and antagonizing the targeted conversion. In multi-metallic systems, forming composite metal oxides ($M_xN_yO_z$) increases the energy barrier for releasing active catalytic ions, hindering carbonate cleavage and leaving unreacted carbonate feedstocks. For detoxification, F and P are effectively immobilized as CaF_2 and $Ca_2P_2O_7$. The relative content of detected gas-phase nitriles is minimized to <2% due to the strong antagonistic effect of Ni^{2+} on Li^+-promoted hexanedinitrile cleavage, while sulfur species derived from 1,3-propane sultone are converted to SO_2 and ultimately mineralized as calcium and metal-sulfur salts. Mechanistically, product distributions and crystallographic properties suggest a hypothesized sequential activation model—$Li^+ \rightarrow Ni^{2+} \rightarrow Mn^{4+}$—governing reactivity, whereas $Co^{2/3+}$ does not participate in the synergistic detoxification and selective upgrading process. This migration–reaction coupling framework provides critical insights for cathode-assisted in situ catalytic pyrolysis and closed-loop electrolyte recycling.

Keywords: spent electrolyte; vacuum catalytic pyrolysis; cathode metals; sequential activation; deep detoxification; directional conversion

Check for updates

Academic Editor: Sascha Nowak

Received: 13 April 2026
Revised: 17 May 2026
Accepted: 21 May 2026
Published: 29 May 2026

Copyright: © 2026 by the authors. Licensee MDPI, Basel, Switzerland. This article is an open access article distributed under the terms and conditions of the Creative Commons Attribution (CC BY) license.

1. Introduction

The rapid expansion of new energy technologies, driven by global commitments to carbon neutrality and energy security, has led to an unprecedented surge in the production and deployment of lithium-ion batteries (LIBs) [1]. As the core component of electric vehicles and energy storage systems, global LIB production is projected to exceed 1 TWh by 2025, while their limited-service life (8–10 years) will result in a massive wave of retired batteries, reaching millions of tons annually by 2030 [2,3]. This transition is shifting the focus of LIB recycling from simple metal recovery toward the holistic management of complex, multi-component waste streams.

Among these components, the electrolyte represents a particularly challenging yet underexplored fraction. Although accounting for only ~10–15 wt.% of LIBs, spent electrolytes constitute the primary source of organic and heteroatom-containing pollutants during recycling [4]. Typical electrolyte systems consist of carbonate solvents, including ethylene carbonate (EC), diethyl carbonate (DEC), and ethyl methyl carbonate (EMC), lithium salts such as lithium hexafluorophosphate ($LiPF_6$), and functional additives such as fluoroethylene carbonate (FEC), 1,3-propane sultone (PS), and hexanedinitrile (ADN), which collectively exhibit high volatility, chemical instability, and strong toxicity [4,5]. Upon exposure to air or thermal treatment, $LiPF_6$ readily decomposes into HF and organophosphorus species, while sulfur- and nitrogen-containing additives generate SO_2 and NO_x during conventional incineration, posing severe environmental and health risks [6,7]. These characteristics render electrolyte detoxification both technically difficult and environmentally critical.

Current treatment strategies, including solvent extraction, incineration, and hydrometallurgical oxidation [6,8–10], are largely limited by incomplete detoxification, secondary pollution, or poor resource valorization. In particular, these approaches typically treat electrolytes as "waste to be removed", rather than as reactive feedstocks with potential for value-added conversion. This paradigm neglects a key opportunity: the intrinsic chemical reactivity and catalytic potential embedded within other battery components.

Notably, spent cathode materials—especially layered ternary oxides, such as $Li(Ni_xCo_yMn_z)O_2$ cathode materials (NCM)—are not inert residues but chemically active materials under thermal and reductive conditions [11–13]. Transition metals such as Ni, Co, and Mn have been widely reported to catalyze cracking, dehydrogenation, and rearrangement reactions of organic molecules, while Li species can participate in nucleophilic and organometallic reaction pathways [14–16]. These properties suggest that cathode materials can act as in situ catalytic agents, enabling a "waste-to-waste synergy" in which toxic electrolyte components are simultaneously decomposed and upgraded. However, despite emerging evidence of catalytic activity, the element-specific roles [17,18], synergistic/antagonistic interactions, and migration-controlled reaction pathways of Li, Ni, Co, and Mn remain poorly understood, particularly under vacuum catalytic conditions. Moreover, the interaction between cathode-derived metal species and acid–base bifunctional catalysts (e.g., CaO-modified ZSM-5) [19–21] has not been systematically elucidated. This knowledge gap limits the rational design of integrated processes for simultaneous detoxification and fuel production.

This study proposes a cathode–zeolite synergistic catalytic framework for the in situ directional conversion of waste LIB electrolytes into light hydrocarbons. By coupling a CaO-modified ZSM-5 catalyst (CaO-ZSM-5*) with model metal species (LiOH, NiO, Co_3O_4, MnO_2) and representative NCM cathode materials under vacuum catalytic pyrolysis conditions, we aim to: (i) elucidate the element-specific catalytic roles of cathode metals (Li, Ni, Co, and Mn) in promoting C–O bond cleavage in carbonates, decarboxylation and oxygen fixation, and the directional conversion into light hydrocarbons; (ii) uncover the synergistic and antagonistic effects of multi-metal interactions (e.g., the formation of composite metal oxides, $M_xN_yO_z$) on the energy barrier for active ion release; and (iii) clarify the mechanisms of deep detoxification, specifically the mineralization of F, P, and S, and the suppression of gas-phase nitriles.

We demonstrate that Li^+ and Ni^{2+} dominate the synergistic detoxification and selective upgrading process by promoting C–O bond cleavage and directional conversion. Conversely, $Co^{2/3+}$ primarily contributes via lattice oxygen release that causes deep oxidation of hydrocarbons, and does not participate in the synergistic detoxification and selective upgrading process. A cathode-dictated sequential activation ($Li^+ \rightarrow Ni^{2+} \rightarrow Mn^{4+}$) governs the reaction pathways, with Mn^{4+} engaging in the later stage for complete sulfur

mineralization, revealing a structure–reactivity relationship intrinsic to cathode materials. Importantly, fluorine, phosphorus, and sulfur species are effectively immobilized as stable inorganic salts (e.g., CaF_2, $Ca_2P_2O_7$, as well as calcium and metal-sulfur salts). Overall, this work establishes a migration–reaction coupling framework and a cathode-assisted self-catalytic paradigm, providing a new strategy for reconciling deep detoxification with directional conversion into light hydrocarbons, thereby enabling closed-loop recycling of lithium-ion batteries.

While our previous work demonstrated the macroscopic feasibility of utilizing spent NCM cathodes for electrolyte defluorination and directional upgrading into light fuels [22], the individual catalytic contributions, multi-metallic interactions, and activation pathways of the constituent metals (Li, Ni, Co, Mn) within the spent cathode materials were not separately deconvoluted. This study systematically investigates these element-specific migration–reaction mechanisms by employing model metal compounds across mono- and multi-metallic configurations over a CaO-ZSM-5* catalyst. The investigation clearly resolves the divergent roles of the metals, identifying that while Li^+ and Ni^{2+} dominate the targeted hydrocarbon conversion, $Co^{2/3+}$ and Mn^{4+} release reactive oxygen species causing deep oxidation. Furthermore, we uncover the suppressive effects of composite metal oxides ($M_xN_yO_z$) on active ion release, the Ni-driven suppression of toxic nitriles, and a cathode-dictated sequential activation order ($Li^+ \rightarrow Ni^{2+} \rightarrow Mn^{4+}$). These findings establish a comprehensive migration–reaction coupling framework, providing distinct complementary insights for closed-loop battery recycling. To explicitly delineate these distinctions, a systematic comparison between our prior work [22] and the present study is provided in Table 1.

Table 1. Comparison of experimental parameters and key outputs between our prior work [22] and the current study.

Parameter	Prior Work	This Manuscript
Feedstock (Waste Stream)	Real spent NCM cathode + PVDF binder + electrolyte	Simulated spent electrolyte
Catalyst Components	CaO + ZSM-5 molecular sieve	Metal Additives (MA: LiOH, NiO, Co_3O_4, MnO_2) + $Ca(OH)_2$ + ZSM-5 molecular sieve
Catalyst Preparation	Energy-intensive multi-step process: (1) Wet mixing in deionized water at 80 °C; (2) Vacuum drying at 110 °C for 12 h; (3) Pre-calcination at 500 °C for 4 h under vacuum.	Simplified two-step physical mixing: (1) Dry mixing ZSM-5 and $Ca(OH)_2$ (2:1 wt.); (2) Blending MA with the base catalyst (1:3 wt.).
Mass Ratios	Electrolyte: CaO-ZSM-5: Cathode = 2:2:1	Metal Additive: Electrolyte: CaO-ZSM-5* = 1:2:3
Process Conditions	Temperature: 530 °C Initial pressure: 100 Pa Pyrolysis time: 20 min	Temperature: 530 °C Initial pressure: 100 Pa Pyrolysis time: 20 min
Research Objective	Macro-level feasibility of electrolyte defluorination and directional upgrading into light fuels	Element-specific mechanistic deconvolution of individual cathode metals and their multi-metallic interactions
Key Outputs/Conclusions	(1) Proof of concept for Li-promoted carbonate cracking (2) Macroscopic defluorination via CaF_2 formation	(1) Divergent roles: Li/Ni promote hydrocarbons; Co/Mn cause deep oxidation via reactive oxygen species. (2) Phase interactions: $M_xN_yO_z$ formation hinders active ion release. (3) Nitrile distribution: Ni strongly antagonizes ADN cleavage. (4) Activation sequence: Cathode-dictated sequential activation ($Li^+ \rightarrow Ni^{2+} \rightarrow Mn^{4+}$).

2. Materials and Methods

2.1. Chemicals and Materials

Spent LIBs containing $LiNi_{1/3}Co_{1/3}Mn_{1/3}O_2$ (NCM) cathode materials were sourced from Shanghai Electric Group Corporation (Shanghai, China). To ensure operational safety, the spent LIBs were discharged in a saturated NaCl solution for 24 h, followed by manual dismantling to retrieve the electrode sheets. Since the direct recovery of spent electrolytes is constrained by high volatility and limited mass fraction, a matrix-assisted diffusion method [22] was adopted. Immediately after disassembly, the recovered electrode sheets were immersed in a commercial ternary electrolyte (KLD-1230C; Canrd, Dongguan, China) to extract the residual components, thereby yielding the simulated spent electrolyte (which intrinsically contains trace stabilizing additives, such as aliphatic amines serving as HF scavengers, standard in commercial formulations).

Gas chromatography-mass spectrometry (GC-MS) analysis of this solution, as characterized in our previous study [22] (Table S1), identified the solvent matrix as ethyl methyl carbonate (EMC, 41.47%), diethyl carbonate (DEC, 22.70%), and ethylene carbonate (EC, 21.04%), alongside 1.0 M $LiPF_6$ (2.29%). Toxic additives, including hexanedinitrile (ADN, 7.37%), fluoroethylene carbonate (FEC, 1.86%), 1,3-propane sultone (PS, 1.75%), and vinylene carbonate (VC, 1.52%), were also quantified, ensuring a rigorous replication of the hazardous waste stream. To systematically decouple the catalytic roles of individual cathode metals, lithium hydroxide (LiOH, 99.95% metals basis; Macklin, Shanghai, China), nickel(II) oxide (NiO, 99.9%; Aladdin, Shanghai, China), cobalt(II,III) oxide (Co_3O_4, 99.5%; Aladdin, Shanghai, China), and manganese(IV) oxide (MnO_2, 99.5%; Aladdin, Shanghai, China) were employed as model compounds to simulate the lithium species and transition metal oxides in the cathode. ZSM-5 molecular sieves (Si/Al ratio = 38; Aladdin, Shanghai, China) and calcium hydroxide ($Ca(OH)_2$, 95.0%; Sinopharm Chemical Reagent Co., Ltd., Shanghai, China) were utilized as catalyst precursors. Carbon tetrachloride (CCl_4, 98%; Rhawn, Shanghai, China), high-purity nitrogen (N_2, 99.999%), and helium (He, 99.999%; Tianyi Gas, Shanghai, China) were also used.

2.2. Experimental Design

Preparation of composite catalysts. A mechanical mixing strategy was adopted to prepare a series of composite catalysts, aiming to elucidate the catalytic mechanism and decouple the specific roles of the metal species inherent in spent NCM cathodes (Li, Ni, Co, and Mn). The base catalyst, designated as CaO-ZSM-5*, was prepared by physically mixing ZSM-5 molecular sieves with $Ca(OH)_2$ in a mortar at a mass ratio of 2:1. $Ca(OH)_2$ was selected to substitute CaO in this study, considering that it not only constitutes the predominant calcium species on the ZSM-5 support but also undergoes in situ thermal conversion to CaO during the pyrolysis process. High-purity metal oxides and hydroxides (LiOH, NiO, Co_3O_4, MnO_2) were selected as model compounds to simulate the characteristic metal species of NCM cathodes, constituting the metal additives (denoted as MA). LiOH was specifically selected because it mimics the residual alkaline layer commonly found on spent cathodes; additionally, any trace water released from its decomposition is kinetically buffered by the massive in situ dehydration of the $Ca(OH)_2$ base matrix. These components were introduced, either individually or in specific combinations, into the catalyst system. For multi-metallic systems (i.e., those containing two or more metal species), the constituent model compounds were homogenized in equal mass fractions prior to integration. The final composite catalysts, collectively denoted as MA-CaO-ZSM-5*, were formulated by blending MA with CaO-ZSM-5* at a fixed mass ratio of 1:3.

To systematically identify potential synergistic or antagonistic interactions, the experimental framework was stratified into five distinct categories: a control group (CaO-ZSM-5*

only), and mono-, bi-, tri-, and tetrametallic systems. The control group was designated as E-0, while the metal-catalyzed groups were designated by the prefix 'E-' followed by the initials of the incorporated metal elements (e.g., E-L, E-LN, up to E-LNCM), with comprehensive specifications detailed in Table S2. Additionally, experimental data for the spent NCM cathode-catalyzed system (designated as Group E) were referenced from our previous work [22] for comparative analysis.

Procedure of synergistic catalytic pyrolysis. The schematic flow of the catalytic pyrolysis process is illustrated in Figure S1. Experiments were conducted in a vacuum tube furnace equipped with a digital pressure gauge. To prevent the premature volatilization of the simulated spent electrolyte, a layered loading strategy was employed. In this arrangement, the electrolyte was placed at the bottom of a quartz boat and immediately covered with a uniform layer of the MA-CaO-ZSM-5* catalyst. The loaded boat was then rapidly transferred into the furnace to minimize exposure. Considering the complexity of the vacuum catalytic pyrolysis process, each experimental group was conducted as a rigorously controlled single experiment. In all MA-catalyzed experiments, the mass ratio of MA, the electrolyte, and CaO-ZSM-5* was fixed at 1:2:3, as detailed in Table S2, and the total mass of the loaded materials in the quartz boat was approximately 6.0 g. For the blank control group (E-0), no metal additive was introduced, and the electrolyte/CaO-ZSM-5* loading followed the corresponding 0:2:3 ratio in Table S2. This standardized loading strategy was implemented to ensure comparable filling levels, heat transfer, and reaction conditions across all experiments. First, the reactor was evacuated to an initial pressure of 100 Pa and then sealed. The temperature was then increased from ambient to 530 °C at a heating rate of 10 °C/min and maintained for 20 min. During this closed pyrolysis process, the reactor operated as a sealed static-vacuum system rather than a continuous-flow or constant-pressure system. Given the relatively small electrolyte loading compared with the large free volume of the quartz tube, the generated pyrolysis gas was not quantified using a calibrated gas-volume measurement device. Subsequently, high-purity nitrogen was introduced to purge the pyrolysis gases into a gas collection bag. The system was immediately re-evacuated to vacuum to expel the remaining carrier gas and prevent secondary reactions. Finally, after the system had cooled to room temperature, the pyrolysis residues were collected, and the pyrolysis oil condensed on the inner wall of the quartz tube was thoroughly recovered using CCl_4 for subsequent characterization. CCl_4 was specifically selected because its lack of C–H and C–O bonds effectively prevents solvent peaks from overlapping with both the unreacted oxygenated electrolyte components and the newly formed pyrolysis products during gas chromatography-mass spectrometry (GC-MS) analysis. All resulting CCl_4-containing waste liquids were strictly collected as halogenated organic waste and disposed of according to standard laboratory safety protocols.

2.3. Analysis Methods

The mass-loss profiles during the catalytic pyrolysis of the simulated spent electrolyte mixed with Li-, Ni-, Co-, and Mn-based composite catalysts (CaO-ZSM-5* combined with individual metal additives: LiOH, NiO, Co_3O_4, or MnO_2) were determined via thermogravimetric analysis (TGA; TG 209 F1 Libra, NETZSCH, Selb, Germany). An Al_2O_3 crucible was charged with 5–10 mg of the formulated mixture for each test. The thermal programming was set to increase from 30 to 800 °C at a heating rate of 20 °C/min, maintained under a continuous purge of high-purity N_2 (30 mL/min).

The gaseous and liquid products derived from the catalytic pyrolysis were collected separately and subjected to qualitative and semi-quantitative analyses using a gas chromatography-mass spectrometry system (GC-MS; GCMS-QP2020 NX, Shimadzu, Kyoto, Japan). Different chromatographic columns and methods were selected for the pyrolysis gas and oil. For

the pyrolysis gas analysis, a DB-PLOT Q capillary column (30 m × 0.32 mm × 10 μm) was utilized. The injection, ion source, and interface temperatures were uniformly maintained at 200 °C, while the column oven was initially held at 40 °C for 2 min, ramped to 200 °C at a rate of 6 °C/min, and subsequently maintained for 15 min. High-purity helium served as the carrier gas at a flow rate of 1.60 mL/min with a split ratio of 10:1. Mass spectra were acquired over a mass-to-charge ratio (m/z) range of 10–300, and a 1.0 min solvent cut time was applied to exclude the N_2 purge gas. For the characterization of the pyrolysis oil, an Rtx-5MS capillary column (30 m × 0.25 mm × 0.25 μm) was employed. The temperatures for the injection port, ion source, and interface were set to 280 °C, 230 °C, and 280 °C, respectively. Helium was used as the carrier gas at a flow rate of 1.23 mL/min with a split ratio of 20:1. The column oven followed a multi-stage program: initially held at 40 °C for 2 min, increased to 200 °C at 6 °C/min (held for 2 min), and further raised to 280 °C at 8 °C/min (held for 10 min). The mass scanning range was set to m/z 33–650, with a 3.0 min solvent delay to protect the detector. Data acquisition and processing were performed using GCMSsolution software (version 4.45, Shimadzu Corporation, Kyoto, Japan), and chemical components were identified by cross-referencing with the National Institute of Standards and Technology (NIST) 2020 mass spectral library, with a similarity index threshold of >70 applied to ensure identification reliability. To ensure analytical accuracy, the N_2 purge gas peak was strictly excluded from the pyrolysis gas data. For the pyrolysis oil, background and impurity peaks identified from a separately analyzed CCl_4 solvent blank were completely removed during data integration. For the semi-quantitative analysis, an area normalization method was employed. This calculation was based solely on the total integrated area of all successfully identified product peaks. These reliably identified components accounted for more than 90% of the total integrated peak area, while unidentified trace peaks and background noise were excluded from this normalization calculation. It should be explicitly noted that these results solely represent the relative contents of the detected products to reflect the compositional changes across different experimental conditions, rather than absolute mass yields or strict elemental balances. In this study, light hydrocarbons refer to C_1–C_6 non-aromatic hydrocarbons detected in the pyrolysis gas.

The phase composition and surface chemical states of the pyrolysis residues were analyzed using X-ray diffraction (XRD; D/MAX 2500 V/PC, Rigaku, Tokyo, Japan; scanning rate, 5°/min; 2θ range, 5–80°) and X-ray photoelectron spectroscopy (XPS; AXIS Ultra DLD, Kratos, Kawasaki, Japan), respectively. Furthermore, the surface morphology and localized elemental distribution of the residues were characterized by field emission scanning electron microscopy coupled with energy-dispersive X-ray spectroscopy (FESEM-EDS; GeminiSEM 300, Carl Zeiss, Oberkochen, Germany).

3. Results and Discussion

3.1. Thermal Behavior and Reaction Window of Electrolyte Catalytic Pyrolysis

To systematically establish the reaction window and investigate the element-specific thermal degradation behaviors, thermogravimetric and derivative thermogravimetric (TG-DTG) analyses of the simulated spent electrolyte mixed with Li-, Ni-, Co-, and Mn-based composite catalysts were conducted. As depicted in Figure 1, the catalytic pyrolysis process of the electrolyte in these catalyst-containing mixtures generally exhibits intense decomposition below 300 °C, followed by distinct mid-to-high temperature degradation pathways depending on the metal catalyst.

Low-temperature decomposition (Stages I and II): Across all four catalytic systems, the primary mass loss occurs in the first two stages. Stage I occurs below 100 °C, featuring sharp DTG peaks at 48.2 °C (Li), 55.0 °C (Ni), 52.8 °C (Co), and 52.8 °C (Mn). This initial stage corresponds to the volatilization of low-boiling-point solvents (e.g., EMC) and initial mild decomposition, accounting for mass losses ranging from 10.09% to 16.66%. Subsequently, Stage

II represents the most drastic thermal degradation phase, spanning approximately 100 °C to 300 °C. The prominent DTG peaks in this region are observed at 129.8 °C (Li), 134.8 °C (Ni), and 144.8 °C (Co and Mn). This major weight loss—constituting 15.44% to 23.15% of the total mass—is primarily attributed to the intense cleavage of bulk carbonate solvents (DEC, EC), the thermal decomposition of $LiPF_6$, and the breakdown of functional additives.

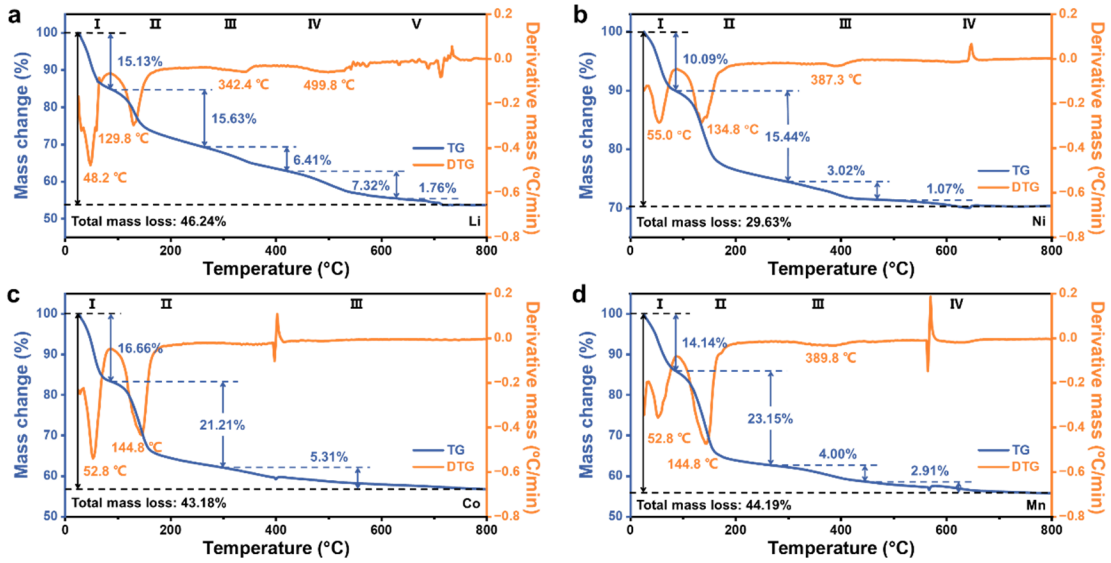


Figure 1. TG-DTG curves of the simulated spent electrolyte mixed with different metal-based composite catalysts: (**a**) LiOH + CaO-ZSM-5*, (**b**) NiO + CaO-ZSM-5*, (**c**) Co_3O_4 + CaO-ZSM-5*, and (**d**) MnO_2 + CaO-ZSM-5*. Roman numerals I–V denote the distinct stages of thermal decomposition.

Mid-to-high temperature degradation (Stages III–V): In the higher temperature regions (>300 °C), the thermal behaviors diverge significantly, reflecting the distinct catalytic activities of the different metal species. The Li-catalyzed system (Figure 1a) exhibits the most prolonged stepwise decomposition, with distinct secondary DTG peaks at 342.4 °C (Stage III) and 499.8 °C (Stage IV), indicating the continuous capability of Li^+ to crack heavier intermediate fragments. In contrast, the Ni and Mn systems (Figure 1b–d) exhibit only minor weight loss peaks around 387.3 °C and 389.8 °C, respectively.

Total mass loss and determination of the reaction window: Ultimately, the total mass loss reaches 46.24% for Li, 43.18% for Co (Figure 1c), and 44.19% for Mn (Figure 1d). Notably, the Ni-catalyzed system (Figure 1b) records a significantly lower total mass loss of only 29.63%. This pronounced difference suggests that Ni promotes the formation of more stable solid carbonaceous residues or heavy inorganic salts within the pyrolysis residue, effectively suppressing the excessive volatilization of mass into the gas phase. Crucially, the TG curves across all four catalytic systems demonstrate that the mass loss processes begin to plateau as the temperature approaches 500 °C. By 530 °C, the derivative mass change (DTG) for all samples approaches zero, indicating that the thermal decomposition reactions of the spent electrolyte are essentially complete. Therefore, to ensure the thorough degradation of the spent electrolyte and provide sufficient reaction severity for its directional conversion under vacuum conditions, 530 °C was determined to be the optimal and sufficient reaction temperature for the subsequent catalytic pyrolysis experiments.

3.2. Role of Individual Metal Elements During In Situ Catalytic Pyrolysis of Electrolyte

3.2.1. Product Comparison Between Monometallic-Catalyzed and Control Pyrolysis

To investigate the specific catalytic roles of the individual metal elements (Li, Ni, Co, and Mn) typical of ternary lithium batteries during the pyrolysis of spent electrolytes, experiments employing CaO-ZSM-5* mixed with individual additives of LiOH, NiO,

Co_3O_4, or MnO_2 (monometallic catalytic systems, designated as groups E-L, E-N, E-C, and E-M, respectively) were conducted. These experiments were performed alongside the CaO-ZSM-5* control group (E-0) at 530 °C and an initial pressure of 100 Pa, with a consistent mass ratio of metal additive to spent electrolyte to CaO-ZSM-5* maintained at 1:2:3. The detailed composition and distribution of the generated pyrolysis gas and oil were analyzed by GC–MS, as presented in Figure 2a and Tables S3 and S4.

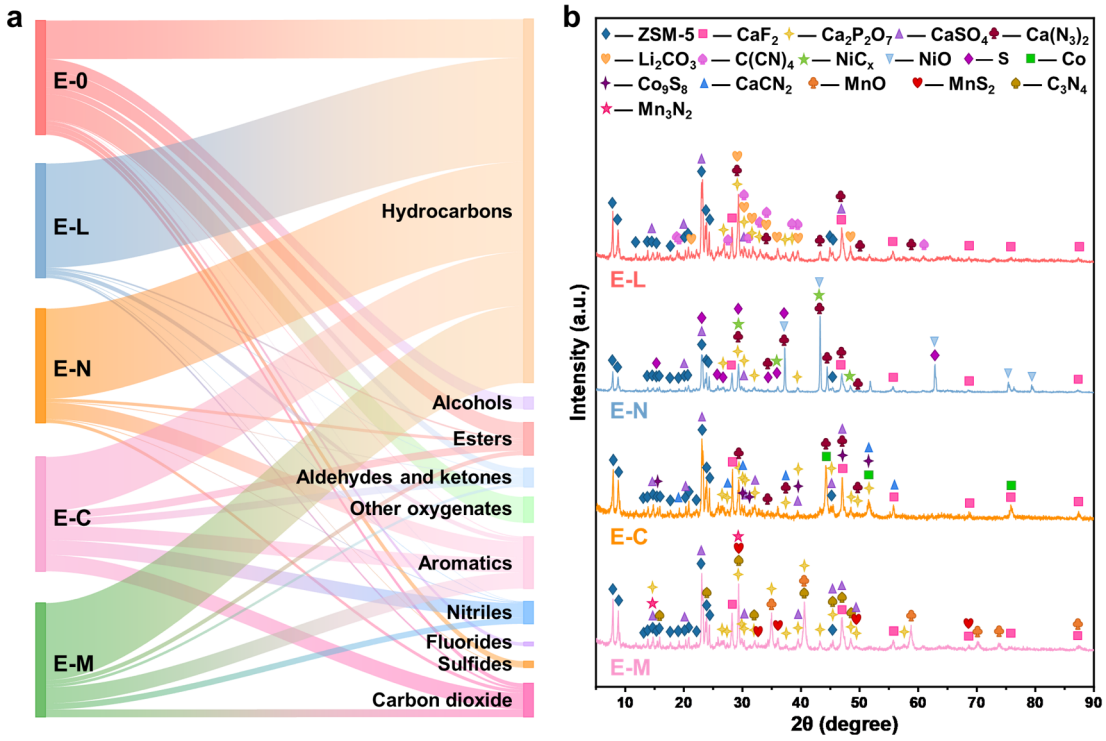


Figure 2. Characterization of pyrolysis product in the reaction system catalyzed by LiOH, NiO, MnO_2, and Co_3O_4 and the blank control group at 530 °C and an initial pressure of 100 Pa. (**a**) The types and content distribution of pyrolysis gases and (**b**) XRD analysis of pyrolysis residue.

Products of control group. For the control group E-0, the pyrolysis gas was dominated by hydrocarbons (33.75%), alcohols (10.57%), esters (14.09%, originating from incomplete pyrolysis of EMC/DEC and carbonates), toxic organics (15.55%), other oxygenates (22.42%), and CO_2 (3.62%). Detailed composition analysis showed that the toxic organics were composed of aldehydes (6.14% acetaldehyde), aromatics (0.93% benzene), nitriles (0.25% 2-propenenitrile), as well as significant amounts of sulfides (5.05%) and fluorides (3.18%). Based on the analysis of elemental composition and molecular structure, the substantial content of esters (14.09%) and remaining oxygenated organics (39.13%, comprising alcohols, aldehydes, and other oxygenates) directly exposes the limitations of the CaO-ZSM-5* catalyst in promoting C–O bond cleavage in carbonates and the decarboxylation/oxygen-fixation of carboxyl-containing compounds, preventing the directional upgrading of spent electrolytes into light hydrocarbons. Meanwhile, the combined content of sulfides and fluorides in the pyrolysis gas reached 8.23%, and small amounts of toxic products such as dimethyl disulfide and 2-(diisopropylamino)ethyl fluoride were detected in the pyrolysis oil of E-0, confirming that CaO-ZSM-5* alone is insufficient for deep detoxification. It is worth noting that the absence of P-containing compounds in both oil and gas phases suggests effective P immobilization within the pyrolysis residues. Additionally, a disproportionately high relative content of tributylamine (87.43%) was detected in the E-0 pyrolysis oil (Table S4). This is not a synthesized product but an intrinsic trace heavy additive from the commercial electrolyte, which was artificially enriched in the relative

area normalization due to the extremely low liquid yield and the lack of metallic cracking catalysts in the blank group.

Products of Li-catalyzed electrolyte pyrolysis. Compared with the control group, Table S3 shows that the addition of LiOH significantly increased the hydrocarbon content in the pyrolysis gas of the E-L group to 91.08%. This significant increase is attributed to the fact that the addition of LiOH promoted the formation of 1-butene, (E)-2-butene, and (Z)-2-butene, with their contents increasing from 7.42%, 3.03%, and 1.06% to 10.69%, 14.19%, and 25.27%, respectively, accompanied by the formation of a large number of newly formed hydrocarbon compounds. Simultaneously, the content of esters and toxic organics decreased to 1.44% and 5.59%, respectively, and alcohols and other oxygenates completely disappeared. Analysis shows that the 12.65% decrease in ester content indicates that Li^+ effectively promoted the breaking of C-O bonds in carbonates, while the 38.55% decrease in the remaining oxygenated organics indicates that Li^+ can also enhance the decarboxylation and oxygen fixation process of carboxyl-containing products catalyzed by CaO-ZSM-5*, ultimately leading to a 57.33% increase in hydrocarbon content in the E-L group. Furthermore, fluorides were not detected in the pyrolysis gas. Regarding sulfur detoxification, the addition of LiOH only reduced the sulfide content in the pyrolysis gas by 4.38%, leaving a 0.67% residue, indicating that Li^+ cannot completely remove sulfur from the pyrolysis gas. However, for the pyrolysis oil (Table S4), no S-containing or fluorinated compounds were detected for the E-L group. There was no significant difference in the content of aromatics and nitriles in the pyrolysis gas between the E-L and E-0 groups, both showing low proportions.

Products of Ni, Co or Mn-catalyzed electrolyte pyrolysis. Compared to group E-0, Table S3 shows that the addition of NiO, Co_3O_4, and MnO_2 also reduced the total ester content in the pyrolysis gas of groups E-N, E-C, and E-M by 11.42%, 7.43%, and 10.16%, respectively; meanwhile, the total content of alcohols, aldehydes, ketones, and other oxygenates decreased by 38.39%, 32.64%, and 36.70%, respectively. Ultimately, this led to increases in hydrocarbon content by 45.02%, 13.42%, and 33.65%, respectively. Based on this analysis, it is believed that Ni^{2+}, $Co^{2/3+}$, and Mn^{4+}, similar to the previously analyzed Li^+, can attack various C–O bond sites within carbonates at high temperatures, cleaving them and synergizing with CaO-ZSM-5* to catalyze the decarboxylation and oxygen fixation of carboxyl-containing products, thereby promoting the targeted conversion of carbonates to light hydrocarbons. No sulfides or fluorides were detected in the pyrolysis gas from the NiO, Co_3O_4, and MnO_2 catalytic systems, indicating that the presence of Ni^{2+}, $Co^{2/3+}$, and Mn^{4+} inhibits the formation of gaseous sulfides and fluorides, which is highly beneficial for the deep detoxification of the spent electrolyte pyrolysis gas phase. Table S4 shows that no fluorinated compounds were detected in the pyrolysis oils of the E-N, E-C, and E-M groups, whereas these metal oxides exhibited different sulfur detoxification capabilities. Co_3O_4 completely removed S from the pyrolysis oil, whereas NiO and MnO_2 were less effective in sulfur removal, with S-containing compounds detected in the pyrolysis oils of the E-N and E-M groups at 6.42% and 15.14%, respectively. Table S3 shows that the addition of NiO, Co_3O_4, and MnO_2 all increased the content of aromatics in the pyrolysis gas by more than 10%. Regarding nitriles, the presence of $Co^{2/3+}$ and Mn^{4+} exhibited a particularly significant impact on their release characteristics in the pyrolysis gas phase. The content of nitriles in the pyrolysis gas of the E-C and E-M groups reached 12.93% and 5.31%, respectively. Compared with the nitrile content of 0.25% in the E-0 group, $Co^{2/3+}$ and Mn^{4+} significantly promoted the generation of gaseous nitriles.

In summary, (1) CaO-ZSM-5* can achieve the complete immobilization of P in the pyrolysis residue; (2) compared with the control group E-0, the analysis results of the monometallic catalytic pyrolysis systems show that: (i) at high temperatures, Li^+, Ni^{2+},

$Co^{2/3+}$, and Mn^{4+} can promote the cleavage of C–O bonds at different sites in carbonates and synergize with CaO-ZSM-5* to achieve the decarboxylation and oxygen fixation of carboxyl-containing products, thereby promoting the directional conversion of carbonates to light hydrocarbons; (ii) for nitriles, the presence of Li^+ and Ni^{2+} has no obvious effect on their gas-phase formation, maintaining a low nitrile content in the pyrolysis gas, whereas $Co^{2/3+}$ and Mn^{4+} significantly promote their gas-phase generation; (iii) for aromatics, the addition of Li^+ does not promote the production of benzene in the gas phase, but Ni^{2+}, $Co^{2/3+}$, and Mn^{4+} all significantly promote the gas-phase generation of aromatics; and (iv) for the gas-phase detoxification of F and S, Li^+, Ni^{2+}, $Co^{2/3+}$, and Mn^{4+} all inhibit the formation of gaseous sulfides and fluorides.

3.2.2. Differences in Catalytic Pyrolysis Products Among Li, Ni, Co, and Mn

Based on the above understanding of monometallic catalytic properties, to explore the differences in the effects of Li^+, Ni^{2+}, $Co^{2/3+}$, and Mn^{4+} in the spent electrolyte vacuum catalytic pyrolysis system, a detailed comparison was conducted on the composition and distribution of the pyrolysis gas and oil, as well as the substances in the pyrolysis residues, among the E-L, E-N, E-C, and E-M groups.

Formation of hydrocarbons and oxygenated organics. As presented in Table S3, the hydrocarbon content in the pyrolysis gas of the E-L, E-N, E-M, and E-C groups decreased sequentially (91.08%, 78.77%, 67.40%, and 47.17%, respectively), while the content of oxygenated organics (comprising esters, aldehydes, and ketones, with no alcohols or other oxygenates detected) increased sequentially (2.02%, 3.41%, 6.36%, and 13.15%, respectively). Additionally, the total content of carbonate raw materials in the pyrolysis oils (Table S4) of the E-L (3.16%), E-N (6.16%), E-M (37.77%), and E-C (57.31%) groups also exhibited an increasing trend. This indicates that the activities of Li^+, Ni^{2+}, Mn^{4+}, and $Co^{2/3+}$ in promoting the cleavage of C–O bonds at different carbonate sites under vacuum conditions, and synergizing with CaO-ZSM-5* to catalyze the decarboxylation and oxygen fixation of carboxyl-containing products, decreased sequentially. However, the low hydrocarbon content of 47.17% in the E-C group is attributed not only to the low activity of $Co^{2/3+}$ in promoting C–O bond cleavage but also to the oxidation of hydrocarbons by reactive oxygen species generated from the high-temperature decomposition of Co_3O_4. Similarly, the reduced hydrocarbon content in the E-M group compared to the E-L/E-N groups is attributed to the aforementioned factors. The generation of reactive oxygen species ultimately led to CO_2 contents reaching 14.28% and 6.86% in the E-C and E-M groups, respectively. This oxidation process is supported by the subsequent XRD and XPS analyses, which indicate the thermal reduction in the initial Co_3O_4 and MnO_2 precursors into lower-valence states (metallic Co^0 and Mn^{2+}), corresponding to the increased relative content of CO_2.

Formation of aromatics and nitriles. Comparisons of aromatics and nitriles were also conducted among the toxic organics. The aromatics content in the pyrolysis gas of the E-L group (3.86%) was significantly lower than that of the E-N (14.21%), E-C (12.47%), and E-M (14.07%) groups, indicating that Li^+ can inhibit the gas-phase formation of aromatics. This further demonstrates that Li^+ effectively promotes the targeted conversion of spent electrolytes into light hydrocarbons. Regarding nitriles, their content in the E-C and E-M groups increased to 12.93% and 5.31%, respectively, compared to 0.48% and 0.71% in the E-L and E-N groups, indicating that Li^+ and Ni^{2+} inhibit the gas-phase formation of nitriles more effectively than $Co^{2/3+}$ and Mn^{4+}. Furthermore, the effects of these metal ions on the gas-phase release of nitriles differed significantly. Analysis of the pyrolysis oil (Table S4) and pyrolysis residues (Figure 2b) revealed that among all monometallic catalytic systems, only the E-N group's pyrolysis oil contained the electrolyte raw material

hexanedinitrile (ADN, 15.09%). This indicates that the activity of Ni^{2+} in promoting ADN pyrolysis is significantly lower than that of the other elements; furthermore, Ni^{2+} promotes the immobilization of a small fraction of ADN pyrolysis products in the pyrolysis residues as $Ca(N_3)_2$, thereby suppressing their gas-phase formation. Although the nitrile content in the pyrolysis gas of the E-L and E-N systems was similar, Li^+ promoted the complete decomposition of ADN and caused the vast majority of the pyrolysis products to couple in the pyrolysis oil and pyrolysis residues, fundamentally suppressing nitrile generation in the gas phase. For the $Co^{2/3+}$ and Mn^{4+} systems, although their pyrolysis oils contained higher N-containing compound contents than the E-L system, and N-containing compounds were detected in the residues of both E-C ($Ca(N_3)_2$, $CaCN_2$) and E-M (Mn_3N_2, C_3N_4) groups, their ability to couple and immobilize ADN pyrolysis products in the pyrolysis residues was significantly weaker than that of Li^+, resulting in a high proportion of nitriles in the pyrolysis gas.

Evolution and immobilization of S- and F-containing species. Li^+, Ni^{2+}, $Co^{2/3+}$, and Mn^{4+} also exhibited distinct characteristics regarding sulfur detoxification. No sulfides were detected in the pyrolysis gas and no S-containing compounds were detected in the pyrolysis oil of the E-C group, while only 0.67% of sulfides were found in the pyrolysis gas of the E-L group. As indicated by Figure 2b, this is attributed to the effective mineralization and immobilization of S in the pyrolysis residues by Li^+ (forming $CaSO_4$) and $Co^{2/3+}$ (forming $CaSO_4$ and Co_9S_8), thereby suppressing the gas-phase formation of sulfides. Similarly, no sulfides were found in the pyrolysis gas of the E-N and E-M systems; however, the content of S-containing organics in their pyrolysis oils reached 6.42% (comprising ethanethiol and PS) and 15.14% (comprising ethanethiol), respectively. This suggests that Ni^{2+} and Mn^{4+} promote the coupling of S-containing gaseous fragments with hydrocarbon fragments in the pyrolysis oil, thereby inhibiting the formation of gaseous sulfides. Naturally, Figure 2b also demonstrates that the mineralization and immobilization of S in the pyrolysis residues of the E-N (as $CaSO_4$ and elemental S) and E-M (as $CaSO_4$ and MnS_2) groups effectively suppressed the gas-phase release of sulfides. Regarding fluorine detoxification, as detailed above, no fluorides were detected in the pyrolysis gas and no fluorinated compounds were detected in the pyrolysis oil for the Li^+-, Ni^{2+}-, $Co^{2/3+}$-, and Mn^{4+}-catalyzed systems, with XRD analysis supporting the mineralization and immobilization of F as CaF_2 across these monometallic systems.

In summary, a comprehensive comparison of the pyrolysis products among the E-L, E-N, E-C, and E-M groups reveals the following: (1) The activities of Li^+, Ni^{2+}, Mn^{4+}, and $Co^{2/3+}$ in promoting the cleavage of C–O bonds in carbonates, and synergizing with CaO-ZSM-5* to catalyze the decarboxylation and oxygen fixation of carboxyl-containing products, decrease sequentially. (2) Compared to Li^+ and Ni^{2+}, the oxygen atoms bound to $Co^{2/3+}$ and Mn^{4+} are more prone to be released from the lattice structure under vacuum conditions, generating reactive oxygen species that lead to the oxidation of hydrocarbons. (3) Regarding aromatics, Li^+ significantly inhibits their gas-phase formation compared to Ni^{2+}, $Co^{2/3+}$, and Mn^{4+}. (4) Regarding nitriles, Li^+ suppresses their gas-phase formation by promoting the coupling of ADN pyrolysis products in the pyrolysis oil and residues. The suppression by Ni^{2+} is primarily attributed to its low catalytic activity for ADN cleavage, whereas $Co^{2/3+}$ and Mn^{4+} significantly promote the gas-phase formation of nitriles. (5) Li^+ and $Co^{2/3+}$ inhibit the generation of gaseous sulfides by promoting the immobilization of PS pyrolysis products in the pyrolysis residues, whereas Ni^{2+} and Mn^{4+} inhibit their gas-phase formation by promoting the coupling of PS pyrolysis products in the pyrolysis oil and residues. (6) Li^+, Ni^{2+}, $Co^{2/3+}$, and Mn^{4+} all showed favorable fluorine detoxification performance, with no fluorides detected in the pyrolysis gas and no fluorinated compounds detected in the pyrolysis oil.

3.3. Synergistic/Antagonistic Effect of Li, Ni, Co, and Mn Multi-Metallic Combination During In Situ Catalytic Pyrolysis of Electrolyte

3.3.1. Bimetallic Antagonism in Hydrocarbon Upgrading

The preceding analysis of the monometallic catalytic systems revealed distinct catalytic advantages and limitations. To explore potential synergistic and antagonistic interactions among these elements, experiments were conducted by mixing CaO-ZSM-5* with pair combinations of the metal additives (bimetallic catalytic systems, designated as groups E-LN, E-LC, E-LM, E-NC, E-NM, and E-CM). Under the same reaction conditions (530 °C, 100 Pa) and mass ratios (1:2:3) as those used in the monometallic catalytic systems, the composition and distribution of the pyrolysis gas and oil were analyzed by GC–MS (Figure 3a and Tables S5 and S6), while the crystal structures of the residues were characterized by XRD (Figure 3b).

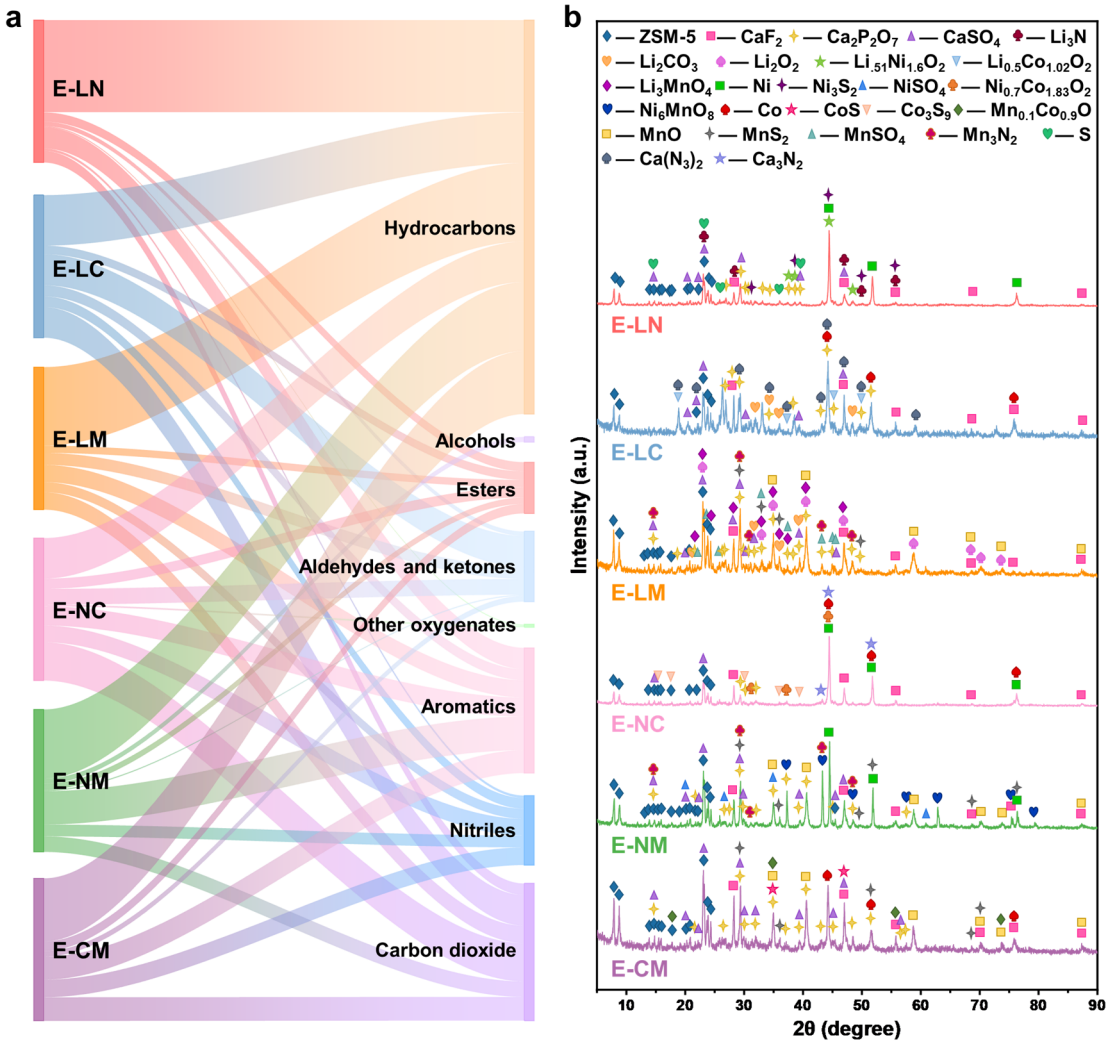


Figure 3. Characterization of pyrolysis product in the reaction system of E-LN, E-LC, E-LM, E-NC, E-NM and E-CM groups at 530 °C and an initial pressure of 100 Pa. (**a**) The types and content distribution of pyrolysis gases and (**b**) XRD analysis of pyrolysis residues.

Regarding the hydrocarbon content in the pyrolysis gas (Figure 3a and Table S5), the bimetallic catalytic systems (E-LN (64.84%), E-LC (35.42%), E-LM (55.10%), E-NC (28.44%), E-NM (48.42%), and E-CM (44.20%)) exhibited significantly lower hydrocarbon contents compared to the monometallic catalytic systems. For instance, in all Li^+-catalyzed bimetallic systems, the introduction of other metal oxides resulted in a 26.24–55.66 percentage-point

decrease in hydrocarbon content for the E-LN, E-LC, and E-LM groups compared to the E-L group. Furthermore, the addition of $Co^{2/3+}$ and Mn^{4+} also led to a sharp decline in hydrocarbon content in the Ni^{2+}-catalyzed systems, and similarly, the introduction of $Co^{2/3+}$ decreased the hydrocarbon content in the Mn^{4+}-catalyzed system. Notably, the hydrocarbon content in the pyrolysis gas of the E-NC group was even lower than that of the control group (E-0). These results suggest an antagonistic trend, where the introduction of metal elements with lower catalytic activities for C–O bond cleavage and decarboxylation/oxygen-fixation was associated with a decrease in the hydrocarbon content of the pyrolysis gas.

XRD results (Figure 3b) reveal that the metal compounds in all bimetallic catalytic systems fused at high temperatures to form composite metal oxides ($M_xN_yO_z$, where M and N represent different elements among Li, Ni, Co, and Mn). The resulting $M_xN_yO_z$ inherently increases the difficulty of releasing active catalytic ions, thereby inhibiting the highly active metals from promoting C–O bond cleavage in carbonates and synergizing with CaO-ZSM-5* to catalyze the decarboxylation and oxygen fixation of carboxyl-containing products.

This deduction is further supported by the high contents of unreacted carbonate raw materials (DEC and EC: 43.65%, 57.51%, 45.15%, 75.61%, 71.42%, and 92.23%) in the pyrolysis oils of the E-LN, E-LC, E-LM, E-NC, E-NM, and E-CM groups (Table S4), as well as the overall increase in the proportions of oxygenated organics in the pyrolysis gas (10.37%, 27.83%, 13.49%, 19.43%, 8.90%, and 10.76%) compared to most monometallic catalytic systems. In terms of structure and composition, the formation of $M_xN_yO_z$ similarly promotes the release of lattice oxygen from NiO, Co_3O_4, and MnO_2, resulting in the deep oxidation of target hydrocarbon products into CO_2 during vacuum catalytic pyrolysis. Consequently, the CO_2 contents in the respective groups reached 8.13%, 21.48%, 12.21%, 26.88%, 10.91%, and 16.55%, further contributing to the reduced hydrocarbon contents.

The gas-phase formation of nitriles and aromatics was also evaluated. Compared to the monometallic catalytic systems, the bimetallic combinations significantly inhibited the generation of naphthalene and o-xylene in the pyrolysis oil, but exhibited a significant promotion effect on the gas-phase formation of aromatics and nitriles. As a result, their combined content in the pyrolysis gas of the E-LN, E-LC, E-LM, E-NC, E-NM, and E-CM groups increased to 16.66%, 15.27%, 19.20%, 25.25%, 31.77%, and 28.49%, respectively.

Furthermore, the consistent detection of unreacted ADN in the pyrolysis oils of all Ni^{2+}- containing bimetallic catalytic systems suggests an antagonistic interaction, where Ni^{2+} may partially inhibit the catalytic activities of Li^+, $Co^{2/3+}$, and Mn^{4+} towards ADN pyrolysis. Notably, Ni^{2+} exhibited the most pronounced inhibitory effect on the catalytic activity of Li^+, as evidenced by the substantial retention of unreacted ADN (39.38%) in the E-LN pyrolysis oil, which consequently resulted in a mere 1.72% of nitriles and only 3.89% of other N-containing compounds in the pyrolysis gas and oil, respectively.

Regarding the detoxification of F and S, all bimetallic catalytic systems showed favorable immobilization of these elements within the pyrolysis residues, with no sulfides or fluorides detected in the pyrolysis gas and no S-containing or fluorinated compounds detected in the pyrolysis oil, suggesting a synergistic trend in heteroatom immobilization among the paired combinations of Li^+, Ni^{2+}, $Co^{2/3+}$, and Mn^{4+} species.

In summary, (1) the formation of composite metal oxides $M_xN_yO_z$ in the bimetallic catalytic combinations: (i) increases the difficulty of releasing active catalytic ions, thereby inhibiting the active metal elements from promoting C–O bond cleavage and synergizing with CaO-ZSM-5* for decarboxylation and oxygen fixation; and (ii) aggravates the release of lattice oxygen from NiO, Co_3O_4, and MnO_2, resulting in the oxidation of hydrocarbon target products. (2) Compared with the monometallic catalytic systems, the bimetallic combinations: (i) inhibit the formation of naphthalene and o-xylene in the pyrolysis oil, but promote the production of aromatics in the pyrolysis gas; (ii) promote the gas-phase

formation of nitriles to varying degrees, although Ni^{2+} strongly antagonizes the catalytic activities of Li^{+}, $Co^{2/3+}$, and Mn^{4+} for ADN pyrolysis (with the Ni^{2+}/Li^{+} antagonism being the strongest, suppressing gas-phase nitriles to below 2% in the E-LN group); and (iii) show a favorable synergistic trend in the detoxification and immobilization of F and S across all bimetallic combinations, as no sulfides or fluorides were detected in the pyrolysis gas, and no S-containing or fluorinated compounds were detected in the pyrolysis oil.

3.3.2. Progressive Suppression in Trimetallic Catalytic Systems

As demonstrated in the bimetallic experiments, the pairing of different metal elements induced distinct interactive catalytic effects. To further dissect the combined catalytic characteristics among these elements in more complex systems, experiments employing CaO-ZSM-5* mixed with ternary combinations of the metal additives (trimetallic catalytic systems, designated as groups E-LNC, E-LNM, E-LCM, and E-NCM, respectively) were conducted. Under the consistent reaction parameters (530 °C, 100 Pa) and mass ratios (1:2:3) maintained across all experimental groups, the detailed composition and distribution of the trimetallic catalytic pyrolysis gas and oil were analyzed by GC–MS (Figure 4a and Tables S7 and S8), while the crystal structures of the residues were characterized by XRD (Figure 4b).

Figure 4a and Table S7 show that the formation of $M_xN_yO_z$ in the trimetallic catalytic pyrolysis systems significantly inhibits the release of active catalytic ions compared to the bimetallic catalytic pyrolysis systems. This hinders the metal elements' ability to promote C–O bond cleavage in carbonates and the synergistic decarboxylation and oxygen fixation of carboxyl-containing products catalyzed by CaO-ZSM-5*, thus impacting the targeted conversion of carbonates to light hydrocarbons. Overall, compared with most of their bimetallic counterparts, the trimetallic catalytic systems showed a further upward trend in the content of oxygenated organics in the pyrolysis gas, reaching 18.67%, 21.82%, 20.05%, and 20.40% for the E-LNC, E-LNM, E-LCM, and E-NCM groups, respectively. Correspondingly, the hydrocarbon content in the pyrolysis gas phase showed an overall downward trend, reaching 48.50%, 39.03%, 26.08%, and 24.50%, respectively. Simultaneously, the total content of carbonate feedstock (EC and DEC) in the pyrolysis oils of the E-LNC, E-LNM, E-LCM, and E-NCM groups (Table S8) reached 57.11%, 66.59%, 79.25%, and 73.35%, respectively. This further confirms that the formation of $M_xN_yO_z$ restricts the conversion of carbonate feedstocks during catalytic pyrolysis.

As for aromatics, similar to the bimetallic catalytic systems, the trimetallic combinations strongly inhibited their formation in the pyrolysis oil, whereas their content in the pyrolysis gas reached 13.66%, 17.94%, 23.59%, and 34.78%, respectively. Compared to the bimetallic catalytic pyrolysis systems, the formation of $M_xN_yO_z$ did not further exacerbate the release of lattice oxygen. Consequently, the CO_2 content in the pyrolysis gas from the trimetallic catalytic systems was comparable to that from the bimetallic catalytic systems containing the same metal elements.

Regarding nitriles, their contents in the pyrolysis gas were similar to those in the bimetallic catalytic systems, and the trimetallic catalytic combinations did not exhibit an inhibitory effect on their formation. Specifically, these compounds still accounted for 4.95%, 7.86%, 6.97%, and 6.42% of the pyrolysis gas in the E-LNC, E-LNM, E-LCM, and E-NCM groups, respectively. Furthermore, all trimetallic catalytic combinations showed a favorable synergistic trend in the detoxification of F and S. No sulfides or fluorides were detected in the pyrolysis gas, and no S-containing or fluorinated compounds were detected in the pyrolysis oil, suggesting that Li^{+}, Ni^{2+}, $Co^{2/3+}$, and Mn^{4+} synergistically promoted the immobilization of these toxic elements within the pyrolysis residues (Figure 4b). A large amount of unreacted ADN was still found in the pyrolysis oils of all Ni^{2+}-containing

trimetallic catalytic systems, which further supports the inference that Ni^{2+} can inhibit the catalytic activities of Li^{+}, $Co^{2/3+}$, and Mn^{4+} towards ADN pyrolysis.

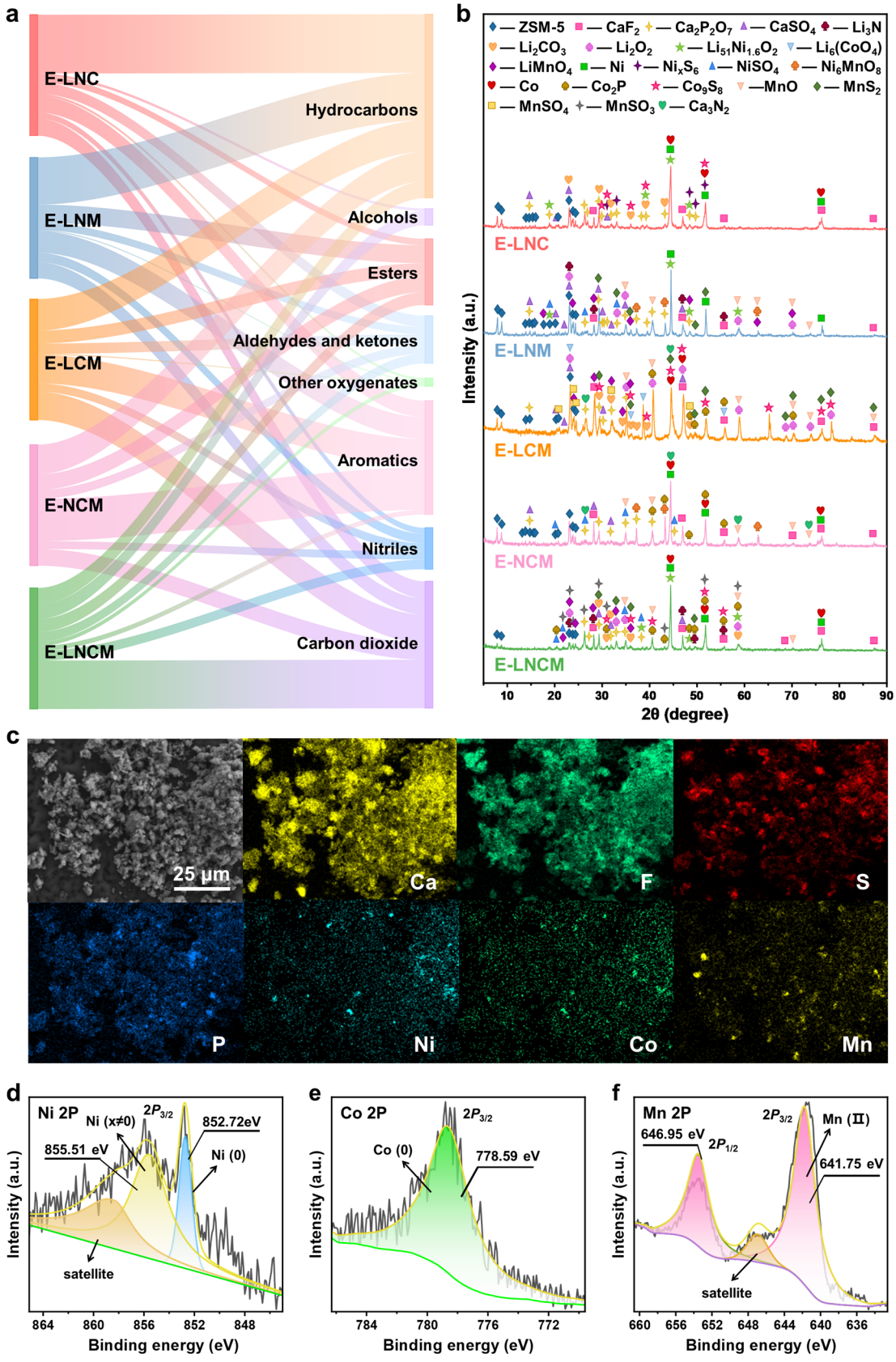


Figure 4. Characterization of pyrolysis products in the reaction system of E-LNC, E-LNM, E-LCM, E-NCM and E-LNCM groups at 530 °C and an initial pressure of 100 Pa. (**a**) the types and content

distribution of pyrolysis gases; (**b**) XRD analysis of pyrolysis residues; (**c**) microscopic morphology and element distribution of the pyrolysis residue of the E-LNCM group; and high-resolution XPS spectra for the surface chemical analysis of (**d**) Ni, (**e**) Co, and (**f**) Mn in the pyrolysis residue of the E-LNCM group. In the high-resolution XPS spectra (**d**–**f**), the black lines represent the raw experimental data, the overall colored smooth lines denote the fitted curves, the lower solid lines indicate the Shirley backgrounds, and the colored shaded areas correspond to the deconvoluted individual peaks.

In summary, (1) compared to the bimetallic catalytic systems, the formation of the composite metal oxides $M_xN_yO_z$ in the trimetallic catalytic pyrolysis systems (i) further increases the difficulty of releasing active catalytic ions, thereby more significantly inhibiting the metal elements from promoting C–O bond cleavage in carbonates and synergizing with CaO-ZSM-5* for the decarboxylation and oxygen fixation of carboxyl-containing products; and (ii) does not have a significant impact on the release of lattice oxygen from NiO, Co_3O_4, and MnO_2. (2) Similar to the bimetallic catalytic systems, the trimetallic combinations still: (i) maintain a strong inhibition on the formation of aromatics in the pyrolysis oil, but promote their enrichment in the pyrolysis gas phase; (ii) fail to exhibit an inhibitory effect on the gas-phase formation of nitriles, although the inhibitory effect of Ni^{2+} on the catalytic activities of Li^+, $Co^{2/3+}$, and Mn^{4+} towards ADN pyrolysis remains evident; and (iii) showed a favorable synergistic trend in the detoxification and immobilization of F and S across all trimetallic combinations, as no sulfides or fluorides were detected in the pyrolysis gas, and no S-containing or fluorinated compounds were detected in the pyrolysis oil.

3.3.3. Analysis of Tetrametallic Catalytic Pyrolysis Products

Composition of pyrolysis gas and oil. To fully evaluate the combined catalytic effects of the cathode metal elements in ternary lithium batteries during vacuum catalytic pyrolysis, an experiment employing CaO-ZSM-5* mixed with the quaternary combination of the metal additives (tetrametallic catalytic system, designated as group E-LNCM) was conducted. Under the consistent reaction parameters (530 °C, 100 Pa) and mass ratio (1:2:3), the detailed composition and distribution of the resulting pyrolysis gas and oil were analyzed by GC-MS (Figure 4a and Tables S7 and S8).

Table S7 shows that the pyrolysis gas of the E-LNCM group is primarily composed of hydrocarbons, alcohols, esters, toxic organics, other oxygenates, and CO_2, with proportions of 13.80%, 11.86%, 10.76%, 20.15%, 3.44%, and 39.99%, respectively. The toxic organics include 7.97% acetonitrile, 5.57% acetaldehyde, 2.55% acetone, and 4.06% benzene. Compared to the mono-, bi-, and trimetallic catalytic pyrolysis systems, the high proportion (34.18%) of oxygenated organics in the pyrolysis gas indicates that the formation of $M_xN_yO_z$ in the tetrametallic catalytic system significantly inhibits the active catalytic ions from promoting C–O bond cleavage in carbonates and synergizing with CaO-ZSM-5* for the decarboxylation and oxygen fixation of carboxyl-containing products. Furthermore, the 39.99% CO_2 content indicates that the formation of $M_xN_yO_z$ in the tetrametallic catalytic system further promotes the release of lattice oxygen from NiO, Co_3O_4, and MnO_2, leading to a significant reduction in the hydrocarbon content in the pyrolysis gas.

Detailed analyses of the toxic organics were also performed. Regarding aromatics, although benzene accounted for only 4.06% of the pyrolysis gas, analysis based on the high CO_2 content suggests that this reduction is attributed to its deep oxidation by reactive oxygen species. As for nitriles, similar to the bimetallic and trimetallic catalytic pyrolysis systems, the tetrametallic catalytic system failed to exhibit an inhibitory effect on their gas-phase formation, and unreacted ADN was still detected in the pyrolysis oil (Table S8). This demonstrates that Ni^{2+} can still inhibit the catalytic activities of Li^+, $Co^{2/3+}$, and

Mn^{4+} towards ADN pyrolysis. Analysis of gas-phase sulfides and fluorides, together with oil-phase S-containing and fluorinated compounds, reveals that the tetrametallic catalytic system exhibits characteristics consistent with the bimetallic and trimetallic catalytic systems, suggesting favorable immobilization of F and S heteroatoms within the pyrolysis residue. To provide a clearer overview of the extensive GC–MS data, the lumped relative contents of key product categories in the pyrolysis gas across the blank control group and metal-catalyzed groups are summarized in Table 2.

Table 2. Lumped relative contents of key product categories in the pyrolysis gas derived from GC–MS analysis.

Groups	Total Light Hydrocarbons (C_1–C_6)/%	Total Oxygenates/%	Aromatics/%	Nitriles/%	Sulfides/%	Fluorides/%	CO_2/%
E-0	33.75	53.22	0.93	0.25	5.05	3.18	3.62
E-L	91.08	2.02	3.86	0.48	0.67	0	1.89
E-N	78.77	3.41	14.21	0.71	0	0	2.90
E-C	47.17	13.15	12.47	12.93	0	0	14.28
E-M	67.40	6.36	14.07	5.31	0	0	6.86
E-LN	64.84	10.37	14.94	1.72	0	0	8.13
E-LC	35.42	27.83	7.76	7.51	0	0	21.48
E-LM	55.10	13.49	12.12	7.08	0	0	12.21
E-NC	28.44	19.43	13.49	11.76	0	0	26.88
E-NM	48.42	8.90	23.46	8.31	0	0	10.91
E-CM	44.20	10.76	16.13	12.36	0	0	16.55
E-LNC	48.50	18.67	13.66	4.95	0	0	14.22
E-LNM	39.03	21.82	17.94	7.86	0	0	13.35
E-LCM	26.08	20.05	23.59	6.97	0	0	23.31
E-NCM	24.50	20.40	34.78	6.42	0	0	13.90
E-LNCM	13.80	34.18	4.06	7.97	0	0	39.99

Note: Total light hydrocarbons correspond to the hydrocarbons category in Tables S3, S5 and S7, which exclude aromatics; total oxygenates exclude CO_2.

Characterization of pyrolysis residue. To preliminarily analyze the pyrolysis residue of the tetrametallic catalytic system, SEM-EDS was used to observe the micromorphology of the E-LNCM sample (Figure 4c) and to examine the surface distribution of F, P, S, and other elements (Ca, Ni, Co, and Mn). The micromorphological characterization revealed that CaO-ZSM-5* and the metal compounds aggregated during the catalytic pyrolysis process, resulting in significant agglomeration. The EDS elemental mapping revealed a strong spatial correlation between the distributions of F, P, and S, and that of Ca. It is preliminarily inferred that, similar to the mono-, bi-, and trimetallic catalytic systems, the F, P, and S in the E-LNCM group's electrolyte bind to Ca and become immobilized via mineralization after catalytic pyrolysis. However, the distributions of F, P, and S did not exhibit obvious spatial overlap with those of Ni, Co, and Mn.

To further determine the chemical forms of the removed F, P, and S, XRD analysis was performed on the pyrolysis residue of the E-LNCM group (Figure 4b). The XRD patterns clearly exhibited distinct diffraction peaks for CaF_2, $Ca_2P_2O_7$, and $CaSO_4$, confirming the inference that F, P, and S bind to Ca and are immobilized via mineralization as calcium salts during the catalytic pyrolysis process. Additionally, weak diffraction peaks corresponding to $NiSO_4$, $MnSO_3$, MnS_2, and Co_9S_8 were detected, indicating that a minor fraction of the sulfur was also mineralized by bonding with the cathode metals. Simultaneously, the XRD results revealed that the metal oxides (NiO, Co_3O_4, and MnO_2) underwent significant phase transformations during the catalytic pyrolysis, as evidenced by the emergence of distinct peaks for metallic Ni, Co, and MnO. Furthermore, the appearance of diffraction

peaks for $Li_{0.51}Ni_{1.16}O_2$ confirms the formation of the composite metal oxide $M_xN_yO_z$ in the tetrametallic catalytic system.

To further clarify the specific changes in metallic elements during the catalytic pyrolysis process, XPS analysis of the surface chemistry of the E-LNCM sample was performed, as shown in Figure 4d–f. The Ni $2p_{3/2}$ spectrum can be deconvoluted into two main peaks, located at approximately 852.72 and 855.51 eV, which are assigned to metallic Ni^0 and oxidized Ni^{x+} species, respectively. This is consistent with the detection of metallic Ni and $Li_{0.51}Ni_{1.16}O_2$ in the XRD results. For Co, the binding energy of the main peak of Co $2p_{3/2}$ is 778.59 eV, indicating that Co exists primarily as metallic Co^0. Although Co_9S_8 is present, its corresponding valence state was not detected by XPS due to its low content, as evidenced by the weak diffraction peaks in the XRD pattern. In addition, the main peaks of Mn $2p_{3/2}$ and Mn $2p_{1/2}$ are located at approximately 641.75 and 646.95 eV, respectively, demonstrating that Mn exists as Mn^{2+}. The decrease in the valence states of these metal elements can be attributed to the reducing action of the pyrolytic carbon and reductive gases generated in the pyrolysis system.

3.4. Mechanism of In Situ Catalytic Pyrolysis for Light Hydrocarbon Conversion and Electrolyte Detoxification by Li, Ni, Co, and Mn Metals in Cathode Materials

Based on the aforementioned analyses, a plausible mechanism for the deep detoxification and directional conversion of spent electrolytes into light hydrocarbons during vacuum catalytic pyrolysis, synergistically driven by the cathode metals and CaO-ZSM-5*, is proposed. To elucidate this synergy, it is essential to first explicitly distinguish the respective contributions of the acid–base catalysis provided by the basic matrix and the specific metal-driven reactions:

Role of Acid–Base Catalysis (CaO-ZSM-5*): The bifunctional CaO-ZSM-5* matrix governs the acid-base neutralization and secondary shape-selective upgrading. Specifically, the strong basic sites provided by CaO act as chemical traps, rapidly neutralizing and mineralizing acidic primary pyrolysis fragments (e.g., capturing HF and $H_xP_yO_z$ to form stable CaF_2 and $Ca_2P_2O_7$). Meanwhile, the acidic sites and the unique microporous structure of the ZSM-5 framework facilitate the secondary dehydration of intermediate alcohols and assist in the decarboxylation of carboxyl-containing fragments. However, as evidenced by the control group (E-0), acid-base catalysis alone is insufficient to initiate the complete cleavage of stable carbonate solvents.

Role of Metal-Driven Reactions (Li, Ni, Co, Mn): The metal species bridge this reactivity gap via strong coordination and redox mechanisms. Metal cations with high Lewis acidity (such as Li^+ and Ni^{2+}) directly polarize and attack the robust C–O and C=O bonds within the carbonate molecules, driving the primary initial cleavage of the electrolyte solvents. Furthermore, specific transition metals govern redox-driven pathways; for instance, $Co^{2/3+}$ and Mn^{4+} facilitate the release of reactive lattice oxygen, leading to deep oxidation, while Ni^{2+} exhibits unique coordination behaviors that antagonize the primary cleavage of ADN.

Building upon these decoupled baseline roles, the detailed migration-reaction coupling mechanism is elucidated as follows:

(1) Li^+ and Ni^{2+}, in synergy with CaO-ZSM-5*, dominate the process of the directional conversion of spent electrolytes into light hydrocarbons during vacuum catalytic pyrolysis.

The specific analysis is as follows: (i) Based on the characteristics of the monometallic catalytic pyrolysis, the activities of Li^+, Ni^{2+}, Mn^{4+}, and $Co^{2/3+}$ in synergizing with CaO-ZSM-5* to promote the directional conversion of electrolytes into light hydrocarbons decrease sequentially. Furthermore, under the conditions of 530 °C and 100 Pa, the hydrocarbon content in the pyrolysis gases of the E-L and E-N groups is highly comparable to that

of the cathode material-catalyzed group (Group E, 87.19%) from our previous study. Thus, it can be preliminarily deduced that Li^+ and Ni^{2+} in the cathode material primarily drive the C–O bond cleavage in carbonates and dominate the synergistic decarboxylation and oxygen fixation of carboxyl-containing intermediates catalyzed by CaO-ZSM-5*, ultimately promoting the conversion of the spent electrolyte into light hydrocarbons. (ii) Compared across catalytic systems with the same number of metal components, the pyrolysis gases from the E-L and E-N groups (among the monometallic systems) and the Li^+/Ni^{2+} co-catalyzed groups (among the multi-metallic systems) consistently exhibited the highest hydrocarbon content. This further corroborates the dominant roles of Li^+ and Ni^{2+} in synergizing with CaO-ZSM-5* for the directional conversion of spent electrolytes into light hydrocarbons. (iii) The comparison of the aromatics content in the pyrolysis gas of the monometallic catalytic systems reveals that Li^+ significantly minimizes the final emission of aromatics into the pyrolysis gas compared to Ni^{2+}, Mn^{4+}, and $Co^{2/3+}$, which aligns with the low aromatics content observed in Group E (0.84%). Across all catalytic systems, Ni^{2+} consistently inhibits the activities of Li^+, $Co^{2/3+}$, and Mn^{4+} towards ADN cleavage, resulting in the retention of unreacted ADN in the pyrolysis oils of all Ni^{2+}-containing systems. This corresponds to the massive amount of unreacted ADN feedstock (42.66%) detected in the pyrolysis oil of Group E. Regarding the gaseous nitriles, despite this antagonistic effect, Ni^{2+} fails to mitigate their abundant emission into the pyrolysis gas in the $Co^{2/3+}$- and Mn^{4+}-containing systems, leading to the detection of abundant nitriles in their pyrolysis gases. This significantly contrasts with the low nitrile content (1.78%) in the pyrolysis gas of Group E, implying that $Co^{2/3+}$ and Mn^{4+} contribute negligibly to the synergistic conversion process. Conversely, the E-LN bimetallic system exhibited the lowest nitrile content and retained a massive amount of ADN in its pyrolysis oil, sharing multiple highly consistent characteristics with the pyrolysis products of Group E. This comprehensive deduction supports the inference that Li^+ and Ni^{2+} dominate the directional conversion of electrolytes into light hydrocarbons in synergy with CaO-ZSM-5*.

(2) The structure of the cathode material itself suggests a sequential activation model for the metal elements.

The specific analysis is as follows: (i) The formation of composite metal oxides ($M_xN_yO_z$) in the multi-metallic catalytic pyrolysis system increases the energy barrier for ion release. Furthermore, under high-temperature vacuum conditions, the inherent properties of the metal ions inevitably cause them to migrate at distinct rates within the metal oxide lattice. Therefore, it is deduced that the Li^+, Ni^{2+}, $Co^{2/3+}$, and Mn^{4+} in the NCM cathode material ($Li(Ni_{1/3}Co_{1/3}Mn_{1/3})O_2$) lattice are activated sequentially to exert their catalytic effects. It should be acknowledged that owing to the technical challenges of rapid thermal quenching and ex situ re-oxidation under the current vacuum setup, this sequential activation is proposed as a deduced model rather than a directly monitored temporal process. (ii) Based on the above analysis, Li^+ and Ni^{2+}, in synergy with CaO-ZSM-5*, dominate the directional conversion of spent electrolytes into light hydrocarbons, whereas $Co^{2/3+}$ and Mn^{4+} contribute negligibly. Consequently, the hydrocarbon content of Group E is theoretically expected to be similar to that of the E-LN group; however, the actual content in the E-LN group is significantly lower. This deviation can be elucidated by the specific relationship observed among the hydrocarbon contents: Group E-N < Group E < Group E-L. When this trend is evaluated alongside the analysis in (i), it suggests that Li^+ initially participates in the catalytic pyrolysis process, and Ni^{2+} subsequently begins to take effect before reaching the critical temperature point for Li^+ to promote ADN cleavage. This sequential activation mechanism plausibly accounts for the intermediate hydrocarbon content of Group E among these three groups. (iii) From the perspectives of ionic interactions and ionic radii, both the strength of the ionic bonds formed between

the cations within the NCM cathode material lattice and O^{2-}, and the ionic radii of these cations, increase sequentially in the order of Li^+, Ni^{2+}, Mn^{4+}, and $Co^{2/3+}$. Consequently, under high-temperature conditions, the migration rates of Li^+, Ni^{2+}, Mn^{4+}, and $Co^{2/3+}$ within the NCM lattice decrease sequentially. This further supports the inference that Li^+ in the cathode material initially participates in the catalytic pyrolysis process, followed by the subsequent activation of Ni^{2+}.

(3) Li^+, Ni^{2+}, and Mn^{4+}, in synergy with CaO-ZSM-5*, dominate the deep gas-phase detoxification of the spent electrolyte during vacuum catalytic pyrolysis.

The specific analysis is as follows: During the deep gas-phase detoxification of the spent electrolyte, catalyzed by the cathode metals in synergy with CaO-ZSM-5*: **(i) Gas-phase detoxification of F.** As detailed in our previous study [22], the removal of F from $LiPF_6$ is entirely attributed to the previously established thermal decomposition and hydrolysis pathway. Meanwhile, FEC is converted to VC at high temperatures, and the HF eliminated during this process subsequently reacts with the CaO supported on ZSM-5 to form CaF_2. The specific reaction is expressed as follows:

$$C_3H_3FO_3 \xrightarrow{\text{high temperature, CaO}} C_3H_2O_3 + CaF_2 + H_2O$$

Additionally, the pyrolysis gas of the E-0 group contained fluoroethane and fluoroethene, which are structurally inferred to result from the complete cleavage of the Cα-O bonds in FEC. However, these fluorinated gases were not detected in any metal-catalyzed systems. This contrast implies that the removal of F from FEC is driven not solely by high temperatures, but also by these metal cations, which promote the cleavage of C–F bonds in some FEC to generate HF, which is subsequently captured by CaO, leading to the immobilization of F as CaF_2 in the pyrolysis residue. **(ii) Gas-phase detoxification of S.** Results from the metal-catalyzed pyrolysis experiments indicate that Ni^{2+}, $Co^{2/3+}$, and Mn^{4+} can immobilize S via mineralization as salts in the pyrolysis residue. However, only $NiSO_4$, NiS, $MnSO_3$, and MnS_2 were detected in Group E, with no sulfur-containing cobalt salts observed. This indicates that $Co^{2/3+}$ does not participate in the detoxification of S during the catalytic pyrolysis of the spent cathode material. Based on the residue analyses across different groups, the detoxification pathway for S in Group E is hypothesized as follows: As established in our previous study, PS is attacked by Li^+ to generate SO_2. Upon its formation, a portion of the SO_2 directly combines with MnO to form $MnSO_3$, while another fraction is reduced by pyrolytic carbon and hydrocarbons to elemental sulfur (S), which undergoes a redox reaction with metallic Ni to yield NiS. Finally, reactive oxygen species generated from the decomposition of the NCM ternary material oxidize the remaining SO_2 to SO_3, which then bonds with Ni on the NCM lattice surface to form $NiSO_4$. **(iii) Gas-phase detoxification of P.** Results from the E-0 group indicate that the CaO-ZSM-5* molecular sieve can effectively remove phosphorus-containing compounds from the pyrolysis gas and oil, immobilizing P via mineralization as $Ca_2P_2O_7$ in the pyrolysis residue. This identical removal and mineralization behavior is maintained in Group E and all metal-catalyzed systems. The absence of any discernible difference in P removal across these groups demonstrates that the gas-phase detoxification of P from the spent electrolyte is governed by the pathway established in our previous study [22]. In this process, the thermal decomposition of $LiPF_6$ generates PF_5, which undergoes successive hydrolysis to generate POF_3 and subsequent acidic intermediates (e.g., H_3PO_4 and $H_4P_2O_7$) that are captured by the CaO support to form $Ca_2P_2O_7$, with no participation from the cathode metals (Li, Ni, Co, and Mn). **(iv) Gas-phase detoxification of nitriles.** Results from the multi-metallic catalytic systems indicate that Ni^{2+} consistently inhibits the ADN cleavage activities of Li^+, $Co^{2/3+}$, and Mn^{4+}. Furthermore, the low nitrile content in the pyrolysis gas and the high retention

of unreacted ADN in the pyrolysis oil of the E-LN group demonstrate that Ni^{2+} almost completely suppresses the Li^+-promoted ADN bond cleavage. Consequently, during the synergistic catalysis dominated by Li^+ and Ni^{2+}, the gas-phase detoxification of nitriles is primarily attributed to this inhibitory effect of Ni^{2+}. Although a minor fraction of ADN still undergoes the thermal cleavage reactions shown below, results from the E-L and E-N groups reveal that Li^+ and Ni^{2+} further promote the coupling of most nitrogen-containing gaseous fragments within the pyrolysis oil and residue. These combined effects account for the exceptionally low nitrile content (1.78%, comprising HCN, C_3H_3N, and C_3H_5N) in the pyrolysis gas of Group E in our previous study [22].

$$NC - C_4H_8 - CN \xrightarrow{\text{high temperature, } Li^+, Co^{2/3+}, Mn^{4+}} C_3H_3N + HCN + C_2H_4$$

$$NC - C_4H_8 - CN \xrightarrow{\text{high temperature, } Li^+, Co^{2/3+}, Mn^{4+}} C_3H_5N + HCN + C_2H_2$$

(4) The structure of the cathode material itself suppresses the release of lattice oxygen at high temperatures.

The specific analysis is as follows: Results from the multi-metallic catalytic systems indicate that NiO, Co_3O_4, and MnO_2 fuse to form composite metal oxides ($M_xN_yO_z$), which intensifies the release of lattice oxygen, thereby causing the deep oxidation of target hydrocarbon products. This phenomenon is attributed to the relatively weak bonding between metal cations and O^{2-} within these simple metal oxide lattices. In contrast to NiO, Co_3O_4, and MnO_2, the NCM cathode material possesses a more stable lattice arrangement governed by a bonding network comprising metal-oxygen ionic bonds and O–O covalent bonds. This robust intrinsic structure is highly conducive to maintaining lattice integrity at high temperatures, thereby suppressing the detachment of lattice oxygen.

In summary, building upon the analyses in our previous study, the mechanism by which cathode metals synergize with CaO-ZSM-5* for the deep detoxification and directional conversion of spent electrolytes into light hydrocarbons during vacuum catalytic pyrolysis is detailed as follows. In the initial stage of the reaction, $LiPF_6$ undergoes thermal decomposition and hydrolysis to generate HF and phosphate compounds. Most of these products react with the CaO supported on the ZSM-5 molecular sieve and are immobilized as CaF_2 and $Ca_2P_2O_7$, respectively. Meanwhile, the remaining portion corrodes the cathode material, releasing a small amount of free Li^+ (Figure 5a), which synergizes with the hydrolysis intermediate POF_3 to dominate the decomposition of linear carbonates in the low-temperature range. In the middle stage of the reaction, as the temperature increases, a large amount of Li^+ in the cathode material lattice overcomes electrostatic attraction and migrates to the crystal surface (Figure 5b). The migrated Li^+ attacks C–O bonds within linear and cyclic carbonates, inducing the random cleavage of these linkages, with PS decomposing to generate SO_2. As heating progresses, prior to reaching the critical temperature for Li^+-promoted ADN cleavage, Ni^{2+} also migrates to the surface, co-promoting the breaking of carbonate C–O bonds while simultaneously suppressing the catalytic activity of Li^+ toward ADN. Simultaneously, the C–F bonds in FEC undergo cleavage under the combined action of Li^+, Ni^{2+}, and high temperature, yielding HF, which subsequently reacts with CaO, immobilizing fluorine within the pyrolysis residue. While Li^+ and Ni^{2+} cleave the carbonates, nickel-containing compounds and the hydrolysis-generated LiOH work with CaO-ZSM-5* to promote the decarboxylation and oxygen fixation of carboxyl-containing products, as well as the targeted transformation of hydrocarbon and alkoxy radicals into light fractions. At this point, the entire vacuum catalytic pyrolysis process, synergistically driven by cathode metals and CaO-ZSM-5* for the directional conversion of the spent electrolyte into light hydrocarbons, is complete. During this selective upgrading

stage, the majority of Ni^{2+} in the pyrolysis system is reduced to metallic Ni by pyrolytic carbon and hydrocarbons. In the later stage of the reaction, upon further heating, Mn^{4+} also overcomes electrostatic attraction, migrates to the crystal surface, and engages in the catalytic system. Similar to Ni^{2+}, most of the Mn^{4+} is reduced to MnO by the same reducing agents. Concurrently, the SO_2 in the pyrolysis gas undergoes a series of reactions with pyrolytic carbon, hydrocarbons, reactive oxygen species derived from the decomposition of the NCM material, metallic Ni, and MnO. These reactions transform SO_2 into elemental S, $NiSO_4$, NiS, $MnSO_3$, and MnS_2, thereby supporting the effective immobilization of sulfur within the pyrolysis residue. By this stage, the catalytic detoxification of the spent electrolyte, driven by cathode metals in synergy with the CaO-ZSM-5* molecular sieve, is accomplished. Notably, the chemical state evolution of $Co^{2/3+}$ is solely attributed to its redox reactions with species such as pyrolytic carbon, and this ion does not participate in the synergistic vacuum catalytic pyrolysis process with CaO-ZSM-5* for the detoxification and selective upgrading of the electrolyte.

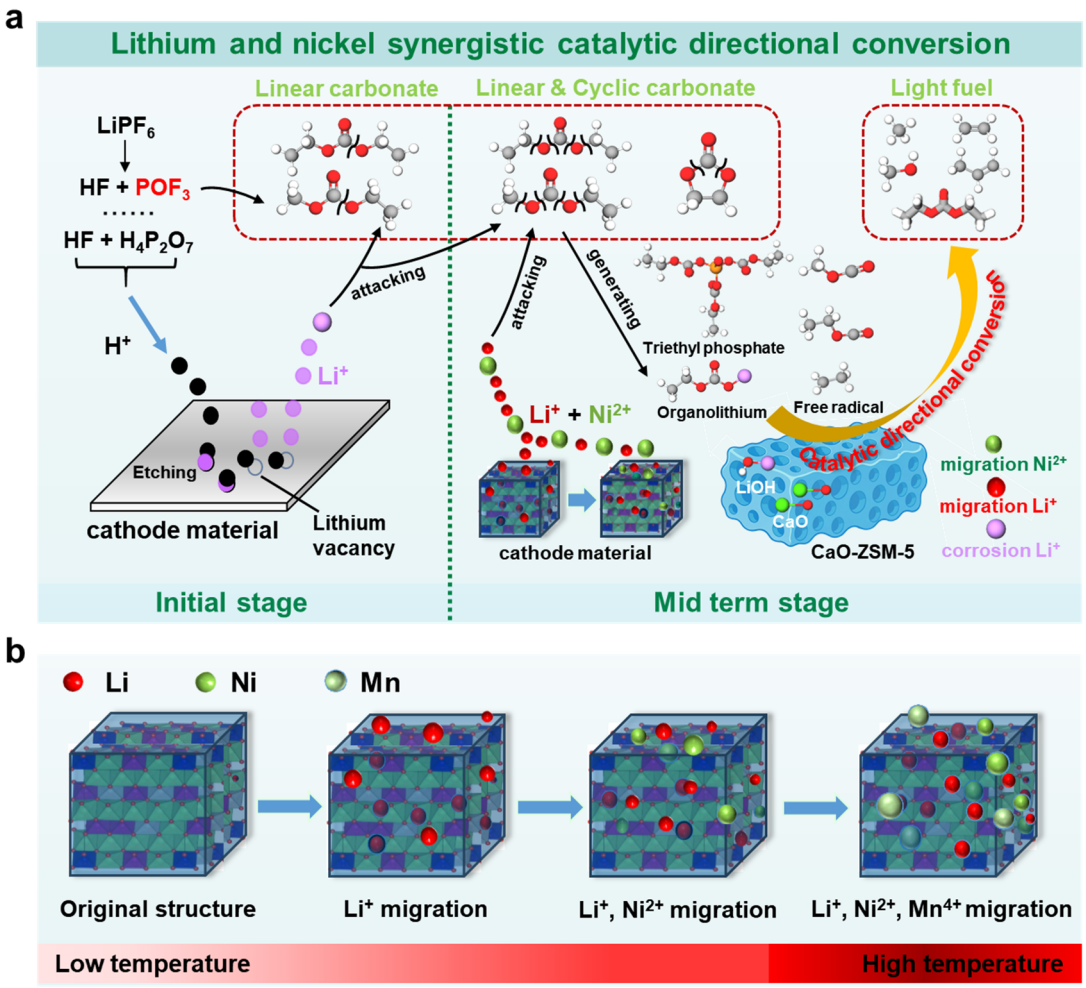


Figure 5. Study of pyrolysis and migration mechanisms of Li^+, Ni^{2+}, and Mn^{4+}. (**a**) Overview of possible mechanisms of Li^+ and Ni^{2+} synergistic CaO-ZSM-5 catalyzed pyrolysis electrolyte directional conversion to light fuel. (**b**) Schematic diagram of the migration characters of Li^+, Ni^{2+} and Mn^{4+} of the lattice of cathode materials with temperature changes. In (**a**), the independent black spheres on the cathode material surface represent H^+ ions, while the dark gray, white, red, and orange spheres in the molecular structures represent carbon (C), hydrogen (H), oxygen (O), and phosphorus (P) atoms, respectively.

4. Conclusions

This study systematically investigates the element-specific, synergistic, and antagonistic effects of cathode metals (Li, Ni, Co, Mn) on the deep detoxification and directional conversion of spent electrolytes into light hydrocarbons over a CaO-ZSM-5* catalyst. Based on batch experiments of vacuum catalytic pyrolysis, a comprehensive migration–reaction coupling mechanism is elucidated. The main conclusions are drawn as follows:

Element-specific catalytic characteristics: At high temperatures, Li^{+}, Ni^{2+}, Mn^{4+}, and $Co^{2/3+}$ promote the cleavage of C–O bonds in carbonates and synergize with CaO-ZSM-5* to achieve the decarboxylation and oxygen fixation of carboxyl-containing products, thereby promoting the directional conversion of carbonates into light hydrocarbons. However, their catalytic activities decrease sequentially in the aforementioned order. Regarding toxic organics, Li+ significantly minimizes the final emissions of aromatics into the pyrolysis gas and reduces nitriles in the pyrolysis gas by promoting the coupling of ADN pyrolysis products in the pyrolysis oil and residues. The minimized emission of nitriles into the pyrolysis gas by Ni^{2+} is primarily attributed to its low catalytic activity for ADN cleavage, whereas $Co^{2/3+}$ and Mn^{4+} significantly promote nitrile release into the pyrolysis gas. For S and F detoxification, Li^{+} and $Co^{2/3+}$ immobilize sulfur in the pyrolysis residues, while Ni^{2+} and Mn^{4+} mitigate final sulfur emissions into the pyrolysis gas by coupling PS fragments in the non-gaseous phases. Ultimately, all these metals showed favorable fluorine detoxification performance, with no fluorides detected in the pyrolysis gas and no fluorinated compounds detected in the pyrolysis oil. Additionally, CaO-ZSM-5* alone can effectively immobilize P as $Ca_2P_2O_7$. Notably, compared to Li^{+} and Ni^{2+}, the lattice oxygen in Co_3O_4 and MnO_2 is more prone to be released under high-temperature vacuum conditions.

Synergistic and antagonistic effects in multi-metallic systems: The formation of composite metal oxides ($M_xN_yO_z$) in multi-metallic systems increases the energy barrier for releasing active catalytic ions, thereby hindering the metal-promoted C–O bond cleavage and the synergistic decarboxylation/oxygen fixation. Furthermore, the high-temperature formation of $M_xN_yO_z$ intensifies the release of lattice oxygen from NiO, Co_3O_4, and MnO_2, causing deep oxidation of hydrocarbon target products. While multi-metallic systems strongly inhibit aromatics in the pyrolysis oil, notable antagonism occurs regarding nitriles: Ni^{2+} significantly inhibits the ADN cleavage activities of Li^{+}, Mn^{4+}, and $Co^{2/3+}$, with the strongest antagonism observed against Li^{+} (suppressing gas-phase nitriles to <2% in the E-LN group while leaving abundant unreacted ADN). However, all multi-metallic combinations showed a favorable synergistic trend in heteroatom immobilization, with no sulfides or fluorides detected in the final gas products and no S-containing or fluorinated compounds detected in the final oil products under the present GC–MS analysis.

Mechanism of migration-reaction coupling in cathode materials: During the early stage of reaction, $LiPF_6$ decomposes, with F and P immobilized in the residues. The hydrolysis intermediate POF_3, synergizing with trace Li^{+} released from corrosion, dominates linear carbonate cleavage at low temperatures. As the temperature rises, guided by the structural constraints of the cathode lattice, a sequential activation of metals occurs. A large amount of Li^{+} first migrates to the lattice surface, initiating the cleavage of carbonate C–O bonds and attacking PS to produce SO_2. Prior to reaching the critical temperature for Li^{+}-promoted ADN cleavage, Ni^{2+} also migrates to the surface, co-promoting carbonate cleavage while strongly antagonizing Li^{+}'s activity toward ADN. Simultaneously, C–F bonds in FEC are cleaved, immobilizing F in the residue. The Li and Ni species then synergize with CaO-ZSM-5* to catalyze decarboxylation, oxygen fixation, and the targeted conversion of radical fragments into light hydrocarbons, accomplishing the selective upgrading process. In the later stages, Mn^{4+} engages in the reactions. SO_2 undergoes complex redox reactions with pyrolytic carbon, hydrocarbons, metallic Ni, MnO, and reactive oxygen species, thereby

promoting the mineralization of S. Notably, $Co^{2/3+}$ does not participate in the synergistic detoxification and selective upgrading process.

Supplementary Materials: The following supporting information can be downloaded at: https://www.mdpi.com/article/10.3390/separations13060163/s1, Figure S1: Schematic diagram of synergistic catalytic pyrolysis process; Table S1: Composition and relative content of the simulated spent electrolyte analyzed by GC-MS (Data are sourced from our previous study); Table S2: Experimental groups and catalyst compositions; Table S3: Composition and relative content (%) of pyrolysis gas in the reaction systems catalyzed by LiOH, NiO, MnO_2, and Co_3O_4 and the blank control group at 530 °C and an initial pressure of 100 Pa; Table S4: Composition and relative content (%) of pyrolysis oil in the reaction systems catalyzed by LiOH, NiO, MnO_2, and Co_3O_4 and the blank control group at 530 °C and an initial pressure of 100 Pa; Table S5: Composition and relative content (%) of pyrolysis gas in the reaction systems catalyzed by bimetallic combinations of LiOH, NiO, MnO_2, and Co_3O_4 at 530 °C and an initial pressure of 100 Pa; Table S6: Composition and relative content (%) of pyrolysis oil in the reaction systems catalyzed by bimetallic combinations of LiOH, NiO, MnO_2, and Co_3O_4 at 530 °C and an initial pressure of 100 Pa; Table S7: Composition and relative content (%) of pyrolysis gas in the reaction systems catalyzed by trimetallic and tetrametallic combinations of LiOH, NiO, MnO_2, and Co_3O_4 at 530 °C and an initial pressure of 100 Pa; Table S8: Composition and relative content (%) of pyrolysis oil in the reaction systems catalyzed by trimetallic and tetrametallic combinations of LiOH, NiO, MnO_2, and Co_3O_4 at 530 °C and an initial pressure of 100 Pa.

Author Contributions: Conceptualization, J.W., Y.Z. and L.Z.; methodology, J.W., Y.Z. and L.Z.; software, J.W.; validation, J.W. and Y.Z.; formal analysis, J.W.; investigation, J.W.; resources, L.Z.; data curation, J.W.; writing—original draft preparation, J.W.; writing—review and editing, J.W.; visualization, J.W. and Y.Z.; supervision, L.Z.; project administration, L.Z.; funding acquisition, L.Z. All authors have read and agreed to the published version of the manuscript.

Funding: This research received no external funding, and the APC was funded by Shanghai University.

Data Availability Statement: The original contributions presented in this study are included in the article/Supplementary Material. Further inquiries can be directed to the corresponding author(s).

Conflicts of Interest: The authors declare no conflict of interest.

References

1. Kang, F.; Zhao, Y.; Liu, Y.; Shen, J.; Liu, W.; Lv, W.; Cao, T.; Cao, H.; Sun, Z. Discharge Pathways and Deactivation Mechanisms of Retired Lithium-Ion Batteries. *ACS Sustain. Chem. Eng.* **2025**, *13*, 5985–5995. [CrossRef]
2. Xing, Z.; Srinivasan, M. Electrochemical Approach for Lithium Recovery from Spent Lithium-Ion Batteries: Opportunities and Challenges. *ACS Sustain. Resour. Manag.* **2024**, *1*, 1326–1339. [CrossRef]
3. Xu, J.; Jin, Y.; Liu, K.; Lyu, N.; Zhang, Z.; Sun, B.; Jin, Q.; Lu, H.; Tian, H.; Guo, X.; et al. A green and sustainable strategy toward lithium resources recycling from spent batteries. *Sci. Adv.* **2022**, *8*, eabq7948. [CrossRef]
4. Mao, Z.; Song, Y.; Zhen, A.G.; Sun, W. Recycling of electrolyte from spent lithium-ion batteries. *Next Sustain.* **2024**, *3*, 100015. [CrossRef]
5. Huang, B.; Pan, Z.; Su, X.; An, L. Recycling of lithium-ion batteries: Recent advances and perspectives. *J. Power Sources* **2018**, *399*, 274–286. [CrossRef]
6. Han, J.Y.; Jung, S. Thermal Stability and the Effect of Water on Hydrogen Fluoride Generation in Lithium-Ion Battery Electrolytes Containing LiPF6. *Batteries* **2022**, *8*, 61. [CrossRef]
7. Liu, M.; Vatamanu, J.; Chen, X.; Xing, L.; Xu, K.; Li, W. Hydrolysis of LiPF6-Containing Electrolyte at High Voltage. *ACS Energy Lett.* **2021**, *6*, 2096–2102. [CrossRef]
8. Xu, R.; Lei, S.; Wang, T.; Yi, C.; Sun, W.; Yang, Y. Lithium recovery and solvent reuse from electrolyte of spent lithium-ion battery. *Waste Manag.* **2023**, *167*, 135–140. [CrossRef]
9. Fernandes, Y.; Bry, A.; de Persis, S. Thermal degradation analyses of carbonate solvents used in Li-ion batteries. *J. Power Sources* **2019**, *414*, 250–261. [CrossRef]
10. Jung, R.; Metzger, M.; Maglia, F.; Stinner, C.; Gasteiger, H.A. Oxygen Release and Its Effect on the Cycling Stability of LiNixMnyCozO$_2$ (NMC) Cathode Materials for Li-Ion Batteries. *J. Electrochem. Soc.* **2017**, *164*, A1361. [CrossRef]

11. Sharifi-Asl, S.; Lu, J.; Amine, K.; Shahbazian-Yassar, R. Oxygen Release Degradation in Li-Ion Battery Cathode Materials: Mechanisms and Mitigating Approaches. *Adv. Energy Mater.* **2019**, *9*, 1900551. [CrossRef]
12. Wu, Z.; Zhang, C.; Yuan, F.; Lyu, M.; Yang, P.; Zhang, L.; Zhou, M.; Wang, L.; Zhang, S.; Wang, L. Ni-rich cathode materials for stable high-energy lithium-ion batteries. *Nano Energy* **2024**, *126*, 109620. [CrossRef]
13. Geldasa, F.T.; Kebede, M.A.; Shura, M.W.; Hone, F.G. Identifying surface degradation, mechanical failure, and thermal instability phenomena of high energy density Ni-rich NCM cathode materials for lithium-ion batteries: A review. *RSC Adv.* **2022**, *12*, 5891–5909. [CrossRef]
14. Li, G.; He, K.; Zhang, F.; Jiang, G.; Zhao, Z.; Zhang, Z.; Cheng, J.; Hao, Z. Defect enhanced CoMnNiOx catalysts derived from spent ternary lithium-ion batteries for low-temperature propane oxidation. *Appl. Catal. B* **2022**, *309*, 121231. [CrossRef]
15. Babii, T.; Jirátová, K.; Balabánová, J.; Koštejn, M.; Michalcová, A.; Maixner, J.; Kovanda, F. Performance of nickel-manganese and nickel-cobalt-manganese mixed oxide catalysts in ethanol total oxidation. *Catal. Today* **2024**, *428*, 114438. [CrossRef]
16. Spannring, P.; Bruijnincx, P.C.A.; Weckhuysen, B.M.; Klein Gebbink, R.J.M. Transition metal-catalyzed oxidative double bond cleavage of simple and bio-derived alkenes and unsaturated fatty acids. *Catal. Sci. Technol.* **2014**, *4*, 2182–2209. [CrossRef]
17. Meng, Z.; Dai, J.; Lu, X.-Y.; Wu, K.; Deng, Y.; Wang, J.; Shih, K.; Tang, Y. Synergetic pyrolysis of lithium-ion battery cathodes with polyethylene terephthalate for efficient metal recovery and battery regeneration. *Commun. Eng.* **2024**, *3*, 175. [CrossRef]
18. Chen, Q.; Zhang, X.; Cheng, R.; Shi, H.; Pei, Y.; Yang, J.; Zhao, Q.; Zhao, X.; Wu, F. Crystal phase and nanoscale size regulation utilizing the in-situ catalytic pyrolysis of bamboo sawdust in the recycling of spent lithium batteries. *Waste Manag.* **2024**, *182*, 186–196. [CrossRef]
19. Chen, X.; Liu, Z.; Chen, W.; Yang, H.; Chen, H. Catalytic pyrolysis of cotton stalk to produce aromatic hydrocarbons over Fe modified CaO catalysts and ZSM-5. *J. Anal. Appl. Pyrolysis* **2022**, *166*, 105635. [CrossRef]
20. Sun, Z.; Xu, B.; Rony, A.H.; Toan, S.; Chen, S.; Gasem, K.A.M.; Adidharma, H.; Fan, M.; Xiang, W. Thermogravimetric and kinetics investigation of pine wood pyrolysis catalyzed with alkali-treated CaO/ZSM-5. *Energy Convers. Manag.* **2017**, *146*, 182–194. [CrossRef]
21. Fu, L.; Xiong, Q.; Wang, Q.; Cai, L.; Chen, Z.; Zhou, Y. Catalytic Pyrolysis of Waste Polyethylene Using Combined CaO and Ga/ZSM-5 Catalysts for High Value-Added Aromatics Production. *ACS Sustain. Chem. Eng.* **2022**, *10*, 9612–9623. [CrossRef]
22. Zhang, Y.; Zhang, X.; Zhu, P.; Li, W.; Zhang, L. Defluorination and directional conversion to light fuel by lithium synergistic vacuum catalytic co-pyrolysis for electrolyte and polyvinylidene fluoride in spent lithium-ion batteries. *J. Hazard. Mater.* **2023**, *460*, 132445. [CrossRef]

Disclaimer/Publisher's Note: The statements, opinions and data contained in all publications are solely those of the individual author(s) and contributor(s) and not of MDPI and/or the editor(s). MDPI and/or the editor(s) disclaim responsibility for any injury to people or property resulting from any ideas, methods, instructions or products referred to in the content.